New Insights into Wind Shear Effects on Entrainment in Convective Boundary Layers Using Conditional Analysis

KATHERINE FODOR

Max Planck Institute for Meteorology, Hamburg, Germany

JUAN PEDRO MELLADO

Universitat Politècnica de Catalunya, Barcelona, Spain

(Manuscript received 17 December 2019, in final form 7 July 2020)

ABSTRACT

Conventional analysis has shown that strong wind shear enhances the entrainment buoyancy flux in the convective boundary layer. By conditioning the entrainment zone into regions of turbulent (i.e., strongly vortical) and nonturbulent (i.e., weakly vortical) flow, some unexpected aspects of this process are revealed. It is found that turbulent regions contribute the most to the entrainment buoyancy flux, but that as wind shear increases, the magnitude of the buoyancy flux in turbulent regions remains approximately constant, or even decreases, despite substantially stronger buoyancy fluctuations. The reason is that the correlation between buoyancy and vertical velocity fluctuations decreases with increasing wind shear, to the extent that it compensates the stronger buoyancy fluctuations. In free convection, this correlation is high because the vertical velocity is mainly determined by the buoyancy force acting in the same direction. Under strong shear conditions, buoyancy is no longer the only external source of vertical velocity fluctuations and their correlation consequently decreases. Hence, shear enhancement of the buoyancy flux in the entrainment zone is primarily due to an increase of the turbulent area fraction, rather than a change of flux inside the turbulent regions.

1. Introduction

Wind shear is well known to modify fluxes at the top of the convective boundary layer (CBL). For weak shear conditions at early states of CBL development, fluxes have been noted to decrease compared to the shear-free CBL (Fedorovich et al. 2001; Conzemius and Fedorovich 2006; Pino and de Arrellano 2008), which may be related to the "shear sheltering" effect described by Hunt and Durbin (1999). The focus of this study, however, is strong shear conditions, which notably enhance fluxes at the top of the CBL. This is commonly attributed to the additional shear production of turbulent kinetic energy (TKE), which acts to increase the magnitude of fluctuations in both the velocity field and thermodynamic properties (Pino et al. 2003; Fedorovich and Conzemius 2008). The growth of the CBL, as well as the evolution of boundary layer clouds, depend crucially on these changes.

One of the more important properties with regard to CBL growth and cloud dynamics is the buoyancy flux. To understand the mechanisms behind shear enhancement of the buoyancy flux, Kim et al. (2003) employed quadrant analysis and found that buoyancy and vertical velocity fluctuations in each quadrant are increased by the large amplitude oscillations of the CBL top induced by strong wind shear.

While quadrant analysis is helpful in determining the sign of fluctuations that contribute to entrainment (Sullivan et al. 1998), other aspects are more difficult to extract. One important issue is external intermittency, which is the property that at the free edge of a turbulent flow, the motion is in some places turbulent and in others not turbulent (Pope 2001). The alternation between turbulent and nonturbulent regions can be seen in visualizations, for example, as a pattern of alternating

regions of high and low vorticity magnitude. In the CBL, external intermittency arises due to the entrainment of weakly vortical air from the free atmosphere and the ascension of strongly vortical thermals from the CBL interior. For convenience, the terms ''turbulent'' and ''nonturbulent'' are commonly used in the atmospheric community to refer to these strongly and weakly vortical regions, respectively, and we adopt that terminology here (Stull 1988; LeMone et al. 2019). While motion within the nonturbulent regions is primarily downward, the turbulent motion within thermals is not unidirectional and hence quadrant analysis, which splits motion into ascending and descending air, is insufficient to distinguish turbulent from nonturbulent regions. As a result, quadrant analysis may be intermingling a number of different wind shear effects.

In the presence of external intermittency, the magnitude of the buoyancy flux is determined by several factors: how large the turbulent area is, how strong the buoyancy flux is in the turbulent regions compared to the nonturbulent regions, and how much mean properties differ between the two regions. This can be expressed analytically as

$$\langle b'w' \rangle = a_T \langle b'w' \rangle_T + a_{NT} \langle b'w' \rangle_{NT} + a_T a_{NT} (\langle b \rangle_T - \langle b \rangle_{NT}) \times (\langle w \rangle_T - \langle w \rangle_{NT}),$$

(1)

where angle brackets denote averaging in the horizontal plane, a_T and $a_{NT} = 1 - a_T$ are, respectively, the turbulent and nonturbulent area fractions, $\langle \cdot \rangle_T$ and $\langle \cdot \rangle_{NT}$ denote the mean inside turbulent and nonturbulent regions, respectively, and $\langle b'w' \rangle_T = \langle bw \rangle_T - \langle b \rangle_T \langle w \rangle_T$ and $\langle b'w' \rangle_{NT} = \langle bw \rangle_{NT} - \langle b \rangle_{NT} \langle w \rangle_{NT}$. Equation (1) will be derived in section 2d. It shows that by taking external intermittency into account, there are several different plausible hypotheses for how wind shear could lead to a stronger buoyancy flux in the entrainment zone:

1) Due to the larger amplitude oscillations of the CBL top, wind shear creates a larger difference in mean properties between turbulent and nonturbulent regions, increasing the term $(\langle b \rangle_T - \langle b \rangle_{NT})(\langle w \rangle_T - \langle w \rangle_{NT})$.
2) Wind shear generates more vigorous fluctuations within the turbulent region, increasing the term $\langle b'w' \rangle_T$.
3) The large-scale structures in the CBL change when wind shear is added, which alters the distribution of turbulent patches in the entrainment zone and thereby a_T and a_{NT}.

Each of these changes can contribute to a larger buoyancy flux, but currently their individual contributions are unknown. Understanding these contributions

could help to improve CBL models (Neggers et al. 2006; Siebesma et al. 2007; Mellado et al. 2017). In this paper, we introduce the method of conditional analysis as a way to understand the interplay between these different contributions toward wind shear enhancement of the entrainment buoyancy flux.

Partitioning of the flow into regions of high and low vorticity magnitude requires the detection of small-scale fluctuations in the enstrophy field. Direct numerical simulation (DNS) has been used with success in this regard for classical flows of engineering importance (Bisset et al. 2002; Mellado et al. 2009; van Reeuwijk and Holzner 2014), as well as in studies of unstratified penetrative convection (Holzner and van Reeuwijk 2017) and gravity currents (van Reeuwijk et al. 2018). Despite DNS gaining traction in the study of sheared CBLs (Jonker et al. 2013; Haghshenas and Mellado 2019), it has not yet been applied in that context in combination with conditioning on turbulent and nonturbulent regions. A further goal of this paper is therefore to assess whether the Reynolds numbers we are able to achieve nowadays with DNS are sufficiently large for this kind of conditional analysis to be useful in the CBL.

Conditioning statistics into turbulent and nonturbulent regions has been used in a variety of canonical flows in fluid mechanics, such as wakes, jets, and turbulent boundary layers (Corrsin and Kistler 1955; Kovasznay et al. 1970; da Silva et al. 2014a). Deardorff et al. (1980) first considered the use of this kind of conditional analysis in laboratory studies of the CBL, noting that a description of the entrainment zone in terms of the turbulent area fraction, rather than in terms of buoyancy profiles, would aid comparison with mechanically driven flows. In the stable boundary layer, partitioning of the flow into turbulent and nonturbulent subvolumes has indicated that properties within turbulent regions remain similar with changing stratification strength (Ansorge and Mellado 2016). By considering the unstable boundary layer here, we help to bridge work across a variety of boundary layer regimes.

This paper is organized as follows. In section 2 we provide an overview of our simulations and the basics of conditional analysis. In section 3 we explain the method we use to partition the flow into turbulent and nonturbulent regions. We then explore how wind shear modifies the turbulent area fraction in section 4 and the buoyancy flux in section 5. A summary is given in section 6.

2. Numerical simulations and analysis methods

We consider a barotropic CBL that is forced by a constant and homogeneous surface buoyancy flux

B_0 and that grows into a linearly stratified free atmosphere. Such conditions are representative of the afternoon atmospheric boundary layer over land. We consider the limit of zero Coriolis parameter. The velocity and buoyancy frequency in the free atmosphere are denoted U_0 and N_0, respectively. Our setup is identical to that in Haghshenas and Mellado (2019), the only difference being that we have continued one of the simulations further into the quasi-steady state of the CBL. Full details of the simulations are given in the aforementioned work, but here we recapitulate the most essential information.

a. Governing equations

We solve the conservation equations for mass, momentum, and energy in the Boussinesq approximation:

$$\nabla \cdot \mathbf{u} = 0 , \tag{2a}$$

$$\frac{\partial \mathbf{u}}{\partial t} + \nabla \cdot (\mathbf{u} \otimes \mathbf{u}) = -\nabla p + \nu \nabla^2 \mathbf{u} + b\mathbf{k} , \tag{2b}$$

$$\frac{\partial b}{\partial t} + \nabla \cdot (\mathbf{u}b) = \kappa \nabla^2 b , \tag{2c}$$

where $\mathbf{u}(\mathbf{x}, t)$ is the velocity vector with components (u, v, w), $\mathbf{x} = (x, y, z)$ is the position vector with z as the vertical coordinate, t is time, $\mathbf{k} = (0, 0, 1)$ is the unit vector in the vertical direction and p is the modified pressure divided by a constant reference density. The buoyancy b is related to the virtual potential temperature θ_v via $b \approx g(\theta_v - \theta_{v,0})/\theta_{v,0}$, where $\theta_{v,0}$ is a constant reference value and g is the gravitational acceleration. The parameters ν and κ are the kinematic viscosity and the thermal diffusivity, respectively.

b. Simulations

All simulations have periodic lateral boundary conditions and are statistically homogeneous in the horizontal directions. The surface is aerodynamically smooth. The velocity field satisfies impermeable, no-slip boundary conditions at the surface and impermeable, free-slip boundary conditions at the top of the domain, which is placed sufficiently far above the CBL to not influence its evolution. An initial velocity field is constructed that is zero at the surface and a constant value in the free atmosphere, U_0, aligned with the x direction.

The buoyancy field satisfies Neumann boundary conditions at both the top and bottom of the domain. At the surface, $\partial_z b = -B_0/\kappa$, and at the top of the domain, $\partial_z b = N_0^2$. The initial buoyancy field is set such that the buoyancy increases linearly with height with gradient N_0^2

in the free atmosphere. The upper 15%–20% of the computational domain contains a sponge layer, which relaxes all profiles back to their initial state, so as to attenuate the reflection of gravity waves.

Once the initial conditions have been sufficiently forgotten, statistical properties in the sheared CBL depend only on the control parameters $\{\nu, \kappa, B_0, N_0, U_0\}$ and, due to statistical homogeneity in the horizontal directions, the independent variables z and t. Dimensional analysis thus dictates that the number of control parameters can be reduced from five to three. Choosing N_0 and B_0 to nondimensionalize the problem, one finds the following three nondimensional control parameters: the Prandtl number, $\mathrm{Pr} \equiv \nu/\kappa$, a reference buoyancy Reynolds number,

$$\mathrm{Re}_0 \equiv \frac{B_0}{\nu N_0^2}, \tag{3}$$

and a reference Froude number,

$$\mathrm{Fr}_0 \equiv \frac{U_0}{N_0 L_0}, \tag{4}$$

where

$$L_0 \equiv \left(\frac{B_0}{N_0^3}\right)^{1/2} \tag{5}$$

is a reference Ozmidov length. The Ozmidov length represents the largest scale at which overturning of eddies is uninhibited by the stratification (Dougherty 1961; Ozmidov 1965). Naturally one can define different Reynolds and Froude numbers using alternative length and velocity scales, such as the boundary layer depth, h, and the convective velocity scale, $w_* = (B_0 h)^{1/3}$ (Deardorff 1970). However, as explained in Haghshenas and Mellado (2019), local scales are important in the entrainment zone, and the scales L_0 and N_0 prove convenient. These local scales might depend on whether one considers the quasi-steady state of a CBL penetrating into a linearly stratified atmosphere, or the case of a strong capping layer, where the buoyancy jump might be more relevant than N_0. We only consider the former case.

The Prandtl number characterizes the properties of the working fluid, the Reynolds number can be thought of as a measure of the scale separation present in the flow (see section 3 for more details) and the Froude number characterizes how strong the wind shear is. We fix the Prandtl number to be equal to one in all of our simulations as this is similar to the Prandtl number of air. Most of our analysis is conducted at

TABLE 1. Simulation properties. The Reynolds number (Re_0) is defined in Eq. (3) and the Froude number (Fr_0) is defined in Eq. (4). The fourth column shows the final time of the simulations. The fifth column shows how the height of minimum buoyancy flux ($z_{i,f}$) varies between $z_{enc}/L_0 = 15$ and the final time of the simulation.

Re_0	Fr_0	Grid	z_{enc}/L_0	$z_{i,f}/z_{enc}$
25	0	$2560 \times 2560 \times 512$	35	1.14–1.14
25	10	$1280 \times 1280 \times 512$	35	1.16–1.15
25	15	$1536 \times 1536 \times 576$	35	1.19–1.16
42	0	$2560 \times 2560 \times 896$	33	1.14–1.14
42	20	$3072 \times 4608 \times 960$	26	1.24–1.16
117	0	$5120 \times 5120 \times 1024$	22	1.15–1.15

$Re_0 = 42$, but in appendix B we assess the Reynolds number dependence of some flow properties, for which we also consider simulations at $Re_0 = 25$ and $Re_0 = 117$. Our analysis compares simulations at $Fr_0 = 0$, a shear-free case, with a simulation at $Fr_0 = 20$, a strong shear case corresponding to wind speeds of around $U_0 = 10$–$15\,\mathrm{m\,s^{-1}}$ for typical midday conditions over land. We will occasionally refer to simulations at $Fr_0 = 10$ and $Fr_0 = 15$ to verify some aspects of wind shear effects, but we do not show the data in the figures for purposes of clarity. In Table 1 we give an overview of the simulations used in this study.

As for the dependence of statistical properties on the independent variables $\{z, t\}$, we use the nondimensional form $\{z/z_{enc}, z_{enc}/L_0\}$. The variable z_{enc} is the encroachment length scale:

$$z_{enc} \equiv \left\{ 2N_0^{-2} \int_0^{z_\infty} [\langle b \rangle(z,t) - N_0^2 z]\, dz \right\}^{1/2}, \qquad (6)$$

where z_∞ is located far enough into the free atmosphere for the integral to be approximately independent of z_∞. In both the shear-free and the sheared cases, z_{enc} characterizes the depth of the mixed layer. By means of an integral analysis of the evolution equation for the buoyancy, Eq. (2c), one obtains the following relationship between the encroachment length and time:

$$\frac{z_{enc}}{L_0} = [2N_0(1 + Re_0^{-1})(t - t_0)]^{1/2}, \qquad (7)$$

where t_0 is a constant of integration. The nondimensional height z_{enc}/L_0, which describes the temporal evolution of the CBL growth, proves convenient to use as opposed to a nondimensional time such as $N_0 t$ because one can estimate it directly from a sounding according to Eq. (6), and it removes the uncertainty introduced by the integration constant t_0 (Garcia and

Mellado 2014). We focus on the quasi-steady regime ($z_{enc}/L_0 \gtrsim 15$), when TKE production is approximately balanced by viscous dissipation, and the time it takes for CBL properties to change significantly is long compared with the turnover time of the large, energy-containing eddies.

In summary, the dependence of statistical properties on $\{\nu, \kappa, B_0, N_0, U_0; z, t\}$ can be expressed in nondimensional form as $\{Re_0, Pr, Fr_0; z/z_{enc}, z_{enc}/L_0\}$. The reason we analyze the system using nondimensional variables is that it removes redundancy, since various combinations of the dimensional parameters can yield equivalent results. This implies that we need only one simulation to cover all possible combinations of the dimensional parameters that yield the same nondimensional parameters. For example, our simulation at $Fr_0 = 20$ could correspond to a day where the free-tropospheric wind speed is $U_0 = 10\,\mathrm{m\,s^{-1}}$, the buoyancy frequency is $N_0 = 10^{-2}\,\mathrm{s^{-1}}$ and the surface buoyancy flux is $B_0 = 2.5 \times 10^{-3}\,\mathrm{m^2\,s^{-3}}$, or equivalently to a day where $U_0 = 15\,\mathrm{m\,s^{-1}}$, $N_0 = 0.75 \times 10^{-2}\,\mathrm{s^{-1}}$ and $B_0 = 4.2 \times 10^{-3}\,\mathrm{m^2\,s^{-3}}$. Moreover, such an approach allows comparisons to be made between atmospheric measurements, physical experiments, and numerical simulations. For instance, a CBL in the real atmosphere with a mixed-layer depth of $z_{enc} = 1$ km, a surface buoyancy flux of $B_0 = 0.5 \times 10^{-2}\,\mathrm{m^2\,s^{-3}}$ and a buoyancy frequency of $N_0 = 0.8 \times 10^{-2}\,\mathrm{s^{-1}}$ is comparable to a tank experiment of a CBL with a mixed-layer depth of $z_{enc} = 0.5$ m, a surface buoyancy flux of $B_0 = 2.5 \times 10^{-5}\,\mathrm{m^2\,s^{-3}}$ and a buoyancy frequency of $N_0 = 2.15 \times 10^{-1}\,\mathrm{s^{-1}}$ because both cases correspond to a state of CBL development of $z_{enc}/L_0 \approx 10$.

We can match typical atmospheric values of all nondimensional parameters except for the Reynolds number. Consequently, simulations at different Reynolds numbers are required to assess the dependence of our results on this parameter (see appendix B).

c. Structure of the entrainment zone

We define the entrainment zone as the region of negative buoyancy flux, which starts at approximately z_{enc} in all cases, and has a two-layer structure (Garcia and Mellado 2014; Haghshenas and Mellado 2019). This distinction into two sublayers helps to explain how entrainment zone properties vary in time and how they depend on environmental conditions. The lower sublayer is located around $z_{i,f}$, the height of minimum buoyancy flux, and the upper sublayer is located around $z_{i,g}$, the height of maximum mean buoyancy gradient. Wind shear thickens the entrainment zone and hence reference heights in the sheared CBL are higher up than in the shear-free CBL.

However, over time, shear effects diminish and the entrainment zone tends toward the convection-dominated regime (see column 5 in Table 1).

The entrainment flux ratio is defined as the minimum of the buoyancy flux normalized by the surface flux: $-\langle b'w'\rangle_{z_{i,f}}/B_0$. Since we are seeking to explain how wind shear increases this quantity, much of our analysis will take place at the height of minimum buoyancy flux.

d. Conditional analysis preliminaries

To investigate how properties differ between turbulent and nonturbulent regions in the entrainment zone and how they evolve over time, we use conditional statistics (Dopazo 1977; Antonia 1981). The conditional mean of a dependent variable ϕ may be expressed as

$$\langle\phi\rangle = a_T\langle\phi\rangle_T + a_{NT}\langle\phi\rangle_{NT}, \tag{8}$$

where, as mentioned in section 1, a_T and $a_{NT} = 1 - a_T$ are, respectively, the turbulent and nonturbulent area fractions, and $\langle\phi\rangle_T$ and $\langle\phi\rangle_{NT}$ are, respectively, the mean inside turbulent and nonturbulent regions. From the definition $\phi' \equiv \phi - \langle\phi\rangle$, one obtains the following expression for the conditional variance:

$$\langle\phi'^2\rangle = a_T\langle\phi'^2\rangle_T + a_{NT}\langle\phi'^2\rangle_{NT} + a_T a_{NT}(\langle\phi\rangle_T - \langle\phi\rangle_{NT})^2, \tag{9}$$

where $\langle\phi'^2\rangle_T = \langle\phi^2\rangle_T - \langle\phi\rangle_T^2$ and $\langle\phi'^2\rangle_{NT} = \langle\phi^2\rangle_{NT} - \langle\phi\rangle_{NT}^2$. The first term on the right-hand side of Eq. (9) is the contribution from the variance inside turbulent regions, the second term is the contribution from the variance inside nonturbulent regions, and the third term is caused by the difference between the mean inside turbulent and nonturbulent regions, hereafter referred to as the mean difference term.

Similarly, one can derive an expression for the vertical flux of ϕ as

$$\langle\phi'w'\rangle = a_T\langle\phi'w'\rangle_T + a_{NT}\langle\phi'w'\rangle_{NT} + a_T a_{NT}(\langle\phi\rangle_T - \langle\phi\rangle_{NT})(\langle w\rangle_T - \langle w\rangle_{NT}). \tag{10}$$

In section 5, we will show how wind shear affects each of the contributing terms in Eq. (10) for $\phi = b$.

3. Definition of turbulent and nonturbulent regions

To proceed with the conditional analysis, we need to define where the flow is turbulent and where it is not. Previous studies have focused on configurations where turbulent regions are embedded in essentially irrotational regions. In such situations, turbulent regions are typically defined based on a low enstrophy threshold, below which the flow may be considered approximately irrotational (da Silva et al. 2014a). In the real atmosphere, however, the free troposphere is not irrotational due, for instance, to gravity waves. Still, the scale separation between the enstrophy values characterizing the boundary layer and those characterizing the free atmosphere is huge (of order 10^6, as explained below). This large scale separation can be used to distinguish between turbulent and nonturbulent regions. Stirring mixing is strongly enhanced in the so-defined turbulent regions compared to the nonturbulent regions, and we want to study the effect of this distinction on entrainment properties. There is one aspect, though, that remains to be ascertained: in our simulations, we can only achieve a limited scale separation between the enstrophy inside the CBL and the enstrophy in the free atmosphere, and in the following sections, we will assess whether this is large enough to make a meaningful distinction between turbulent and nonturbulent regions.

Although we do not study the turbulent/nonturbulent interface itself, we do draw upon previous work on the matter, which, as mentioned, typically defines turbulent regions based on a low enstrophy threshold. Due to the intrinsic arbitrariness associated with choosing a threshold, in this study we consider a range of different thresholds. For the sake of clarity of figures, however, in the main part of the text, we mostly show results at a single reference threshold. Discussion of the dependence of our results on the chosen threshold may be found in appendix A.

Various methods for selecting an enstrophy threshold have been employed in past studies of the turbulent–nonturbulent interface. One method commonly employed in shear-driven boundary layers is to find a range of thresholds where the turbulent volume fraction is insensitive to changes in the threshold (da Silva et al. 2014b; Watanabe et al. 2018). This is closely related to the structure of the probability density function (PDF) of enstrophy, which has two peaks connected by a plateau: one above the boundary layer at low enstrophy values, indicating the nonturbulent region, and one within the boundary layer at high enstrophy values, indicating the turbulent region (Borrell and Jiménez 2016). In shear-driven boundary layers, the plateau in the enstrophy PDF corresponds to where the turbulent volume fraction becomes insensitive to the threshold (Watanabe et al. 2018). Thus, a threshold can equivalently be chosen by locating the saddle point in the PDF. The physical meaning of a threshold

chosen in this way then becomes clear: it divides between enstrophy values more likely to be found in the boundary layer and enstrophy values more likely to be found outside of it.

The enstrophy PDF in the CBL has a similar structure to that in the shear-driven boundary layer, albeit with a reduced scale separation. As already indicated before, this is due to the presence of gravity waves in the free atmosphere, which themselves possess vorticity. For this reason, some authors have suggested using the potential vorticity as a turbulence indicator for stratified flows, as in the absence of diffusion, gravity waves possess zero potential vorticity (Riley and Lelong 2000; Watanabe et al. 2016). In appendix C, we show that the potential vorticity only results in a marginal increase in scale separation in our simulations and it also turns out to be a rather unsuitable turbulence indicator in the CBL, but in any case, our conclusions remain similar even when using it as a conditioning variable. In the following, we therefore only consider conditioning on enstrophy.

We first define a reference enstrophy scale in the mixed layer in order to normalize the PDFs. This can be derived from the relationship between enstrophy, ω^2, and the viscous dissipation rate of TKE, ε:

$$\langle \varepsilon \rangle = \nu \langle \omega^2 \rangle + 2\nu \frac{\partial^2 \langle \omega^2 \rangle}{\partial z^2}, \tag{11}$$

which simplifies to

$$\langle \varepsilon \rangle \approx \nu \langle \omega^2 \rangle, \tag{12}$$

because the second term on the right-hand side of Eq. (11) is small in the mixed layer. It then follows that

$$\langle \omega^2 \rangle \sim \frac{\langle \varepsilon \rangle}{\nu} \sim \frac{B_0}{\nu}, \tag{13}$$

where the last relation follows from an integral analysis of the TKE evolution equation in the quasi-steady regime of the CBL (Fedorovich et al. 2004). We therefore define a reference enstrophy scale in the mixed layer as

$$\omega_0^2 \equiv \frac{c_\varepsilon B_0}{\nu}. \tag{14}$$

This reference scale is verified in Fig. 1 with $c_\varepsilon = 0.1$. We note that the definition of ω_0^2 in Eq. (14) in terms of B_0 and ν is appropriate for the convectively driven boundary layer, and is analogous to the standard definition used in purely shear-driven boundary layers in terms of the friction velocity (Borrell and Jiménez 2016).
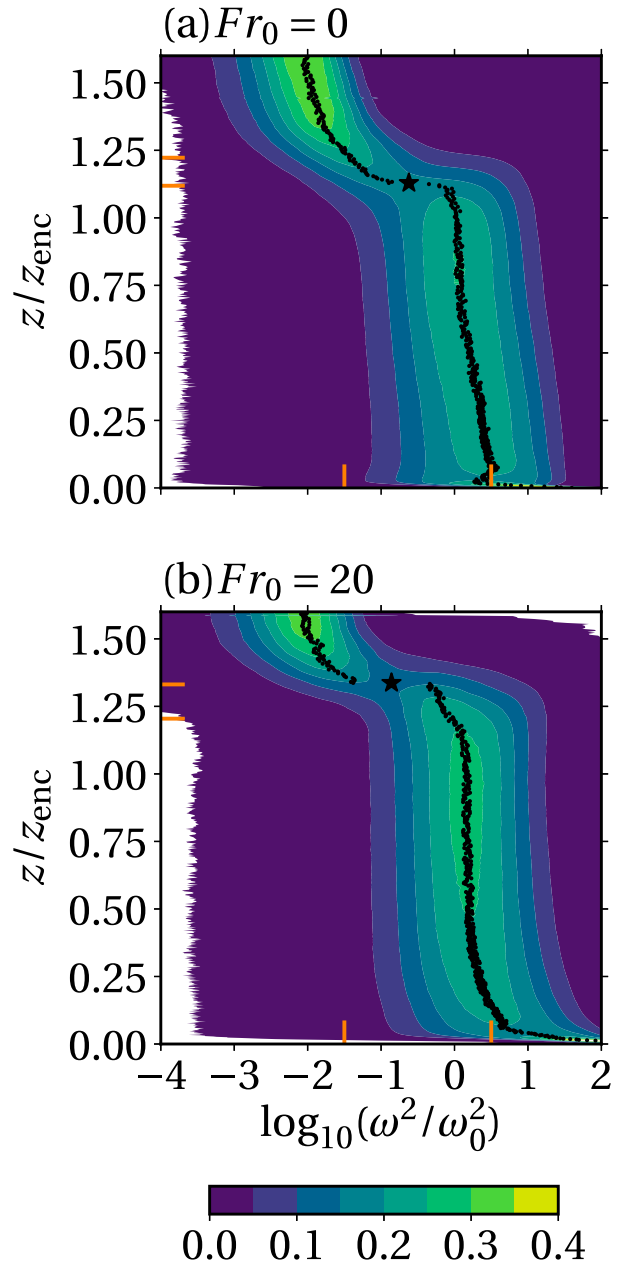

FIG. 1. Probability density functions of enstrophy at $z_{enc}/L_0 = 20$ averaged over an interval $\Delta z_{enc}/L_0 = 2$. The black dots indicate the mode of the PDF at each height. The star shows the approximate saddle point. The lower and upper orange markers on the left-hand side indicate $z_{i,f}$ and $z_{i,g}$, respectively. The orange markers on the bottom axis indicate the range of enstrophy thresholds considered in this study. The reference scale ω_0^2 is defined in Eq. (14) with $c_\varepsilon = 0.1$.

Under typical midday conditions in the real CBL, $B_0 \approx (0.3–1) \times 10^{-2}$ m^2 s^{-3} and $\nu = 1.5 \times 10^{-5}$ m^2 s^{-1}, yielding enstrophy values in the mixed layer of order 10–10^3 s^{-2} (for c_ε of order 0.1–1). In the free atmosphere, which is dominated by gravity wave motion, the
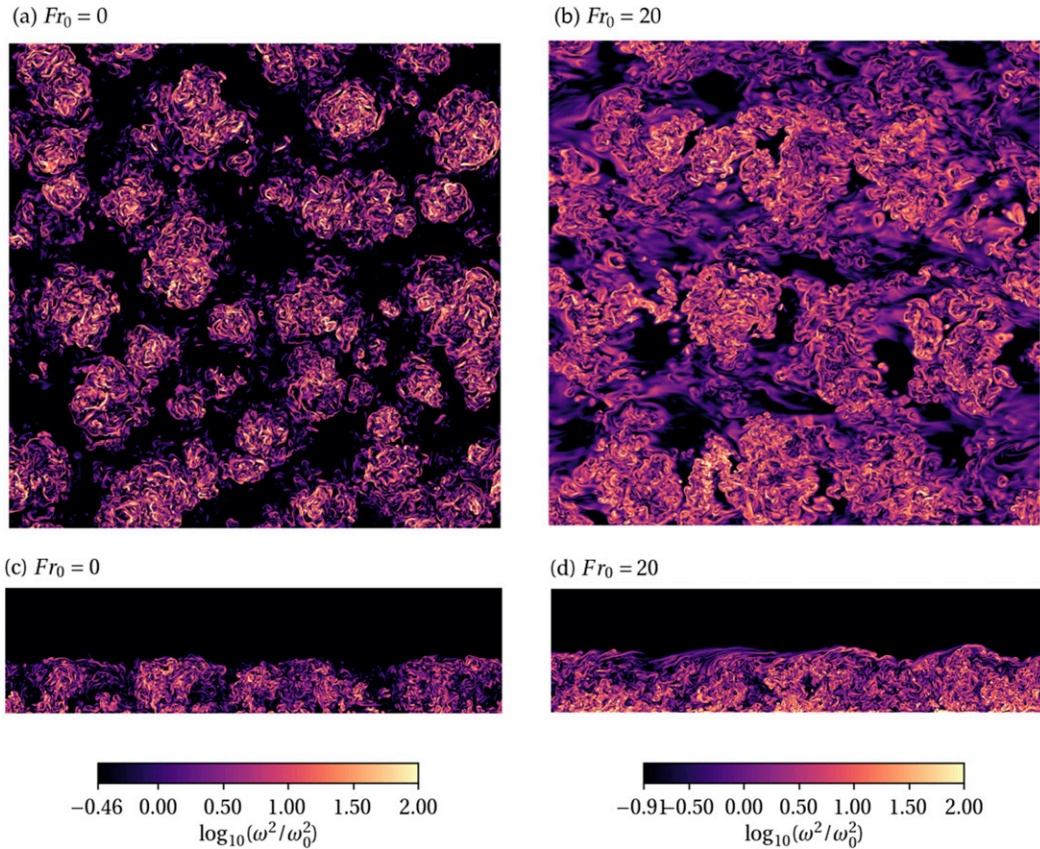
FIG. 2. Cross sections of the enstrophy logarithm at time $z_{enc}/L_0 = 20$. (a),(b) x–y cross sections at the height of minimum buoyancy flux, (c),(d) x–z cross sections in the central y plane. (a),(c) $Fr_0 = 0$ and (b),(d) $Fr_0 = 20$ (mean wind from left to right). The color scale has black as the threshold indicated by the star in Fig. 1. The full horizontal domain is shown and is equal to $215L_0 \times 215L_0$ in both cases.

enstrophy scales with $N_0^2 \approx (0.4$–$3.2) \times 10^{-4} \, s^{-2}$. Hence, the scale separation between the boundary layer and free atmosphere, $\omega_0^2/N_0^2 \approx Re_0$, is of order 10^5–10^7, demonstrating that the scale separation increases with increasing Reynolds number (see also appendix B). In numerical simulations, however, the Reynolds number and the corresponding scale separation in the flow determine how many grid points are required, and thereby the size of the simulation. This is strongly constrained by computational resources and we are therefore limited to Reynolds numbers much smaller than those characterizing the real atmosphere (Mellado et al. 2018). As observed in Fig. 1, in our simulations at $Re_0 = 42$, we only achieve a scale separation of order 10^2. Nonetheless, this is sufficient to make a distinction between turbulent and nonturbulent regions, as will be demonstrated in later sections.

As previously mentioned, the intrinsic arbitrariness associated with choosing a threshold to distinguish turbulent from nonturbulent regions warrants the consideration of a range of thresholds. We show this range in Fig. 1 through the orange ticks on the bottom axis. The highest threshold value roughly corresponds to the mean enstrophy value in the mixed layer, while the lowest threshold value corresponds to an enstrophy value slightly larger than that characterizing gravity waves in the free atmosphere. In section 4 we further justify this range of thresholds.

For conciseness and to better see the effects of wind shear, we focus our main discussion based on one reference threshold. To identify a reference threshold for our analysis, we find an approximation to the saddle point in the enstrophy PDF as follows. First, we find the mode of the PDF at each height (the black dots in Fig. 1). Then, we search along that set of points for where there is a jump in enstrophy values between two consecutive grid points. The size of this jump has to be tuned somewhat depending on the case. We choose the size of the jump to be a factor of at least $1.5 \times \omega^2/\omega_0^2$ in the $Fr_0 = 0$ case and a factor of at least $3 \times \omega^2/\omega_0^2$ in the $Fr_0 = 20$ case. The saddle point is then approximated as the mean value between the points on either side of the jump (the star in Fig. 1).

To give a visual impression of turbulence defined by the reference threshold, in Fig. 2 we show horizontal and

vertical cross sections of the enstrophy field. Enstrophy values below the reference threshold are blacked out and what remains has the characteristic features of turbulent plumes in the shear-free case (Figs. 2a,c) and of horizontal rolls in the sheared case (Figs. 2b,d).

One of the main effects of wind shear is to increase the height of the saddle point from $z_{i,f}$ to $z_{i,g}$. The correspondence of the saddle point to these reference heights is seen more clearly in Fig. 3a. While it is expected that the saddle point in the enstrophy PDF lies within the entrainment zone, it is not obvious why it should lie so close to a reference height based on the mean buoyancy profile or the buoyancy flux profile. Comparing with simulations at $Re_0 = 25$ for the intermediate Froude numbers $Fr_0 = 10$ and $Fr_0 = 15$ (not shown), we find that the saddle point hovers around $z_{i,f}$ in the $Fr_0 = 10$ case, supporting the finding of Haghshenas and Mellado (2019) that wind shear effects are only present above $Fr_0 = 10$. In the $Fr_0 = 15$ case, the saddle point is around $z_{i,g}$, but does not follow it so closely as in the $Fr_0 = 20$ case. In particular, the height of the saddle point does not decrease as much over time as does $z_{i,g}$. This suggests that there is not a strict relation between the height of the saddle point in the enstrophy PDF and the reference heights in the entrainment zone based on buoyancy profiles.

While it is unclear how to explain the exact location of the saddle point in each case, it is possible to explain the *relative* location of the saddle point from one case to another. The saddle point is higher up in the sheared CBL because the turbulence intensity only starts to decay around the height $z_{i,f}$ (Fig. 1b). This is because the height of maximum shear production of TKE is close to $z_{i,f}$ and hence turbulence continues to be generated up to this height. In the shear-free CBL by contrast, turbulence starts to decay upon entering the stably stratified entrainment zone (i.e., slightly above z_{enc}; Fig. 1a), as there is no turbulence production mechanism there. Consequently, the saddle point in the enstrophy PDF occurs lower down.

The magnitude of the enstrophy saddle point is similar between the two cases, though slightly smaller in the sheared case due to the saddle point being closer to the nonturbulent region (Fig. 3b). The reference threshold we use for each Fr_0 case in the following sections is the mean value of the respective curve in Fig. 3b.

4. Turbulent area fraction

One of the most important variables in the conditional analysis we perform is the turbulent area fraction, a_T [see Eq. (1)]. As we will see, this property is also the one
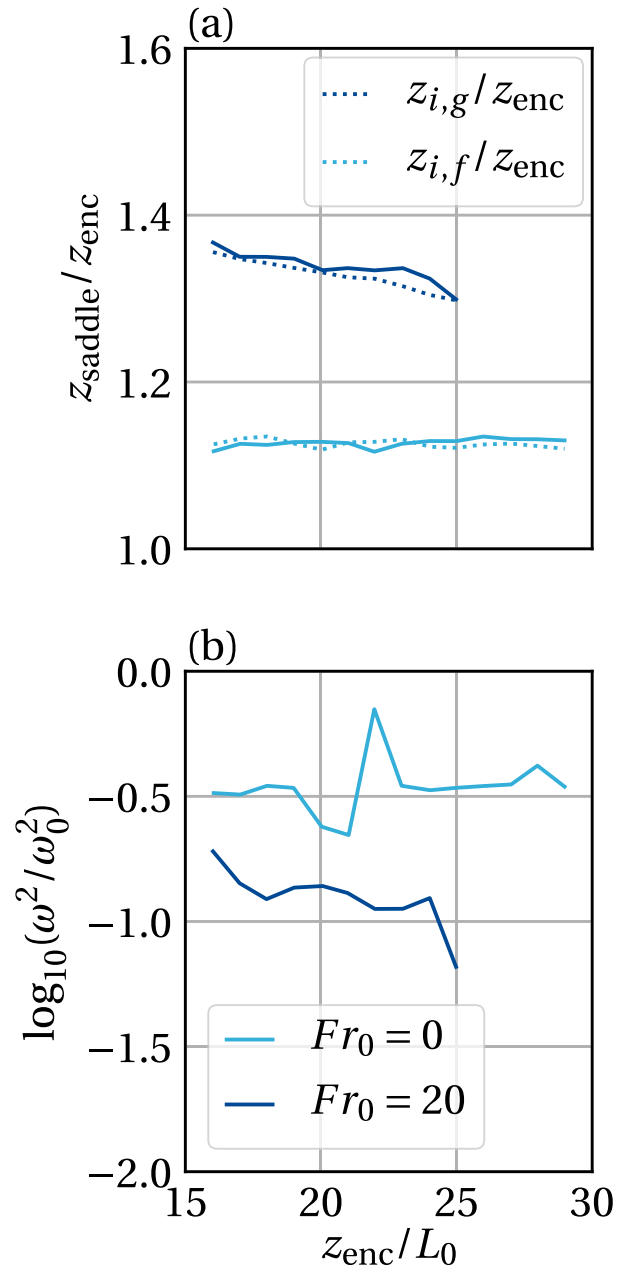

FIG. 3. Time evolution of the location of the saddle point in the enstrophy PDF: (a) height of the saddle point and (b) enstrophy value of the saddle point. Here and in the following, lines indicate the average over an interval $\Delta z_{enc}/L_0 = 2$.

most directly affected by the definition of turbulent and nonturbulent regions. We therefore evaluate how changes to the enstrophy threshold impact the turbulent area fraction, while still maintaining our primary goal of investigating wind shear effects.

In Fig. 4, we show the turbulent area fraction a_T as a function of height and threshold. The structure of these profiles mirrors the structure of the PDFs considered in
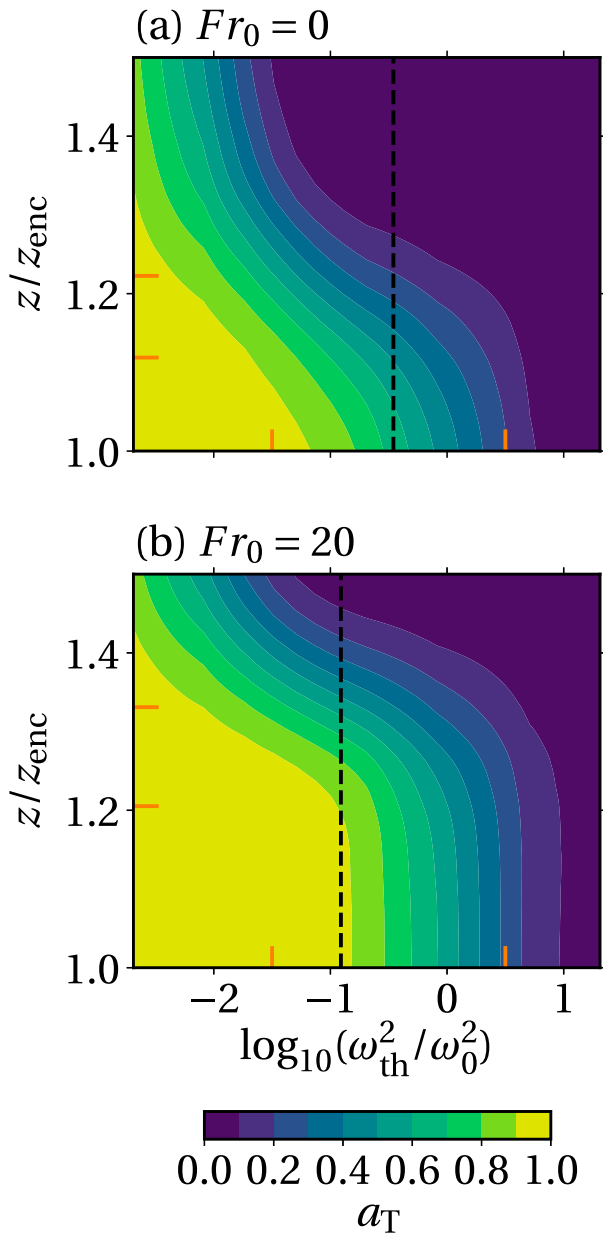
FIG. 4. Contour plots of turbulent area fraction as a function of height and enstrophy threshold at $z_{enc}/L_0 = 20$. The contours are averages over an interval $\Delta z_{enc}/L_0 = 2$. The black dashed line indicates the reference threshold (the mean value of the saddle point in Fig. 3b). The lower and upper orange markers on the left-hand side indicate $z_{i,f}$ and $z_{i,g}$, respectively. The orange markers on the bottom axis indicate the range of enstrophy thresholds considered in this study.

the previous section. Turbulence starts to decay with height as soon as it enters the entrainment zone in the shear-free case, and maintains a constant value up to $z_{i,f}$ in the sheared case.

While it is important to assess how properties change with the threshold, it is equally important to

realize that not all thresholds are physically meaningful. In particular, if the threshold is so high that nowhere is considered turbulent, then $a_T \rightarrow 0$ in the intermittent region. On the other hand, if the threshold is so low that everywhere is considered turbulent, then $a_T \rightarrow 1$ in the intermittent region. In both these cases, the conditional statistics become mathematically equivalent to the conventional statistics, as can be seen from Eqs. (8)–(10), and the conditioning thus loses any physical meaning. For this reason, we only consider thresholds that result in $0.1 < (a_T)_{z_{i,f}} < 0.9$ in the shear-free CBL as physically plausible. From Fig. 4a, we can estimate the corresponding interval of enstrophy thresholds to be $-1.5 \lesssim \log_{10}(\omega_{th}^2/\omega_0^2) \lesssim 0.5$, indicated in Fig. 4 by the orange ticks on the bottom axis (also shown in Fig. 1). Within this range, which spans two orders of magnitude, a comparable threshold on enstrophy in the shear-free and sheared cases always results in a higher turbulent area fraction in the sheared case at the same reference height. Thus, while changing the threshold alters the magnitude of turbulent and nonturbulent properties, the relationship between the shear-free and sheared cases remains qualitatively the same. This is shown to hold in appendix A for a number of different properties.

By considering properties at a single threshold, we can better see the effects of wind shear. For our reference threshold defined in section 3, wind shear increases the turbulent area fraction in the mixed layer by around 15%, but in the entrainment zone the effects are more significant (Fig. 5a). We see in Fig. 5b that at $Fr_0 = 20$, the turbulent area fraction at $z_{i,f}$ has increased by around 70% of the shear-free value. Since the thresholds used are comparable between $Fr_0 = 0$ and $Fr_0 = 20$, we attribute this increase of turbulence coverage to the changing structure of convective plumes (see Fig. 2). Indeed, if the same threshold value used in the $Fr_0 = 20$ case were used in the $Fr_0 = 0$ case, the turbulent area fraction at $z_{i,f}$ would increase, but still not exceed that in the sheared case (see Fig. 4). Wind shear thus definitively spreads turbulence over a wider area in the entrainment zone.

One might imagine that the spreading of turbulence under sheared conditions is related to the well-known transition from convective cells to streamwise rolls. The formation of horizontal roll vortices in the moderately convective boundary layer was detected early in observations and are sometimes visible in the form of cloud streets, indicating that the structures pervade right up to the top of the boundary layer (LeMone 1973). This was later rationalized by Khanna and Brasseur (1998), who, through extensive visualizations from large-eddy simulation (LES), showed that "coherent sheetlike updrafts
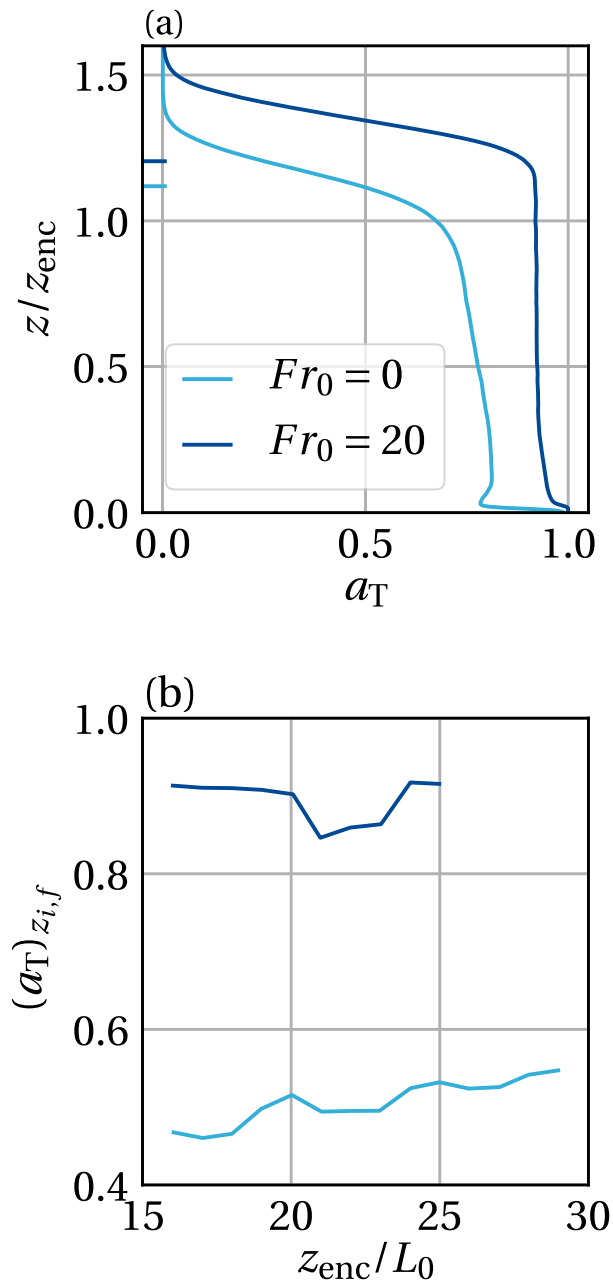
FIG. 5. Turbulent area fraction as a function of (a) height at $z_{enc}/L_0 = 20$ and (b) time at $z_{i,f}$. The threshold used in each case is the mean value of the respective curve in Fig. 3b. The markers on the left-hand side in (a) indicate $z_{i,f}$.

during the time period $15 \lesssim z_{enc}/L_0 \lesssim 26$, indicating that the CBL is indeed in the regime where streamwise roll vortices have been found to exist.

Still, one could ask whether the change of organization from cells to rolls necessarily implies a larger turbulent area fraction at the height of minimum buoyancy flux. The answer to this question is perhaps less to do with organization and more to do with the TKE budget. In the shear-free CBL, the buoyancy flux term, that was a source of TKE in the mixed layer, becomes a sink term in the entrainment zone. Turbulence is not generated in the entrainment zone in this case, it is only transported from the mixed layer. Thus, turbulence starts to decay very quickly inside the entrainment zone (see Fig. 1a) and hence the turbulent area fraction immediately starts to reduce from its mixed-layer value (Fig. 5a). In the sheared CBL by contrast, shear production of turbulence in the entrainment zone causes the turbulent area fraction to remain high.

Based on Fig. 5a, one might think that $(a_T)_{z_{i,f}}$ in the $Fr_0 = 0$ case is only smaller than in the $Fr_0 = 20$ case because the mixed-layer turbulent area fraction is smaller. However, this is not true. If a lower enstrophy threshold were chosen in the $Fr_0 = 0$ case in order to enforce the same mixed-layer turbulent area fraction as in the $Fr_0 = 20$ case (i.e., $-1.5 \lesssim \omega_{th}^2/\omega_0^2 \lesssim -1$), the rapid decay of turbulence in the entrainment zone would still result in a smaller turbulent area fraction at $z_{i,f}$ (see Fig. 4). Moreover, a smaller mixed-layer turbulent area fraction in the shear-free CBL is consistent with the observation that free-tropospheric air can be carried deep into the boundary layer by large-scale downdrafts without too much mixing (Lohou et al. 2010; van de Boer et al. 2014; Fodor et al. 2019). This effect is more prominent in the shear-free CBL, where the descending branches of the convection cells are much less rotational than the ascending turbulent plumes (Fig. 2c). Wind shear facilitates plume merging in the mixed layer (Fig. 2d) and hence the greater turbulence coverage in the sheared CBL.

Figure 5b bears a strong resemblance to the evolution of the total buoyancy flux at $z_{i,f}$ over time at different Fr_0 (see Fig. 5a in Haghshenas and Mellado 2019). This already suggests that the turbulent area fraction may be a key variable in controlling the magnitude of the entrainment flux under different shear conditions, lending support to the third hypothesis in section 1. We explore this possibility further in the following section.

5. Wind shear effects on the buoyancy flux

Using the reference threshold defined in section 3, we show each of the three terms in Eq. (1) as a function of

turn at the capping inversion to form the often-observed large-scale streamwise roll vortices.'' In a more recent LES study, Salesky et al. (2017) showed that roll-type organization in the CBL exists up to values of the mixed-layer stability parameter of $-z_i/L = 15–20$, where z_i is the CBL depth and L is the Obukhov length. In our simulations at $Fr_0 = 20$, $-z_{i,f}/L$ varies between 7 and 21
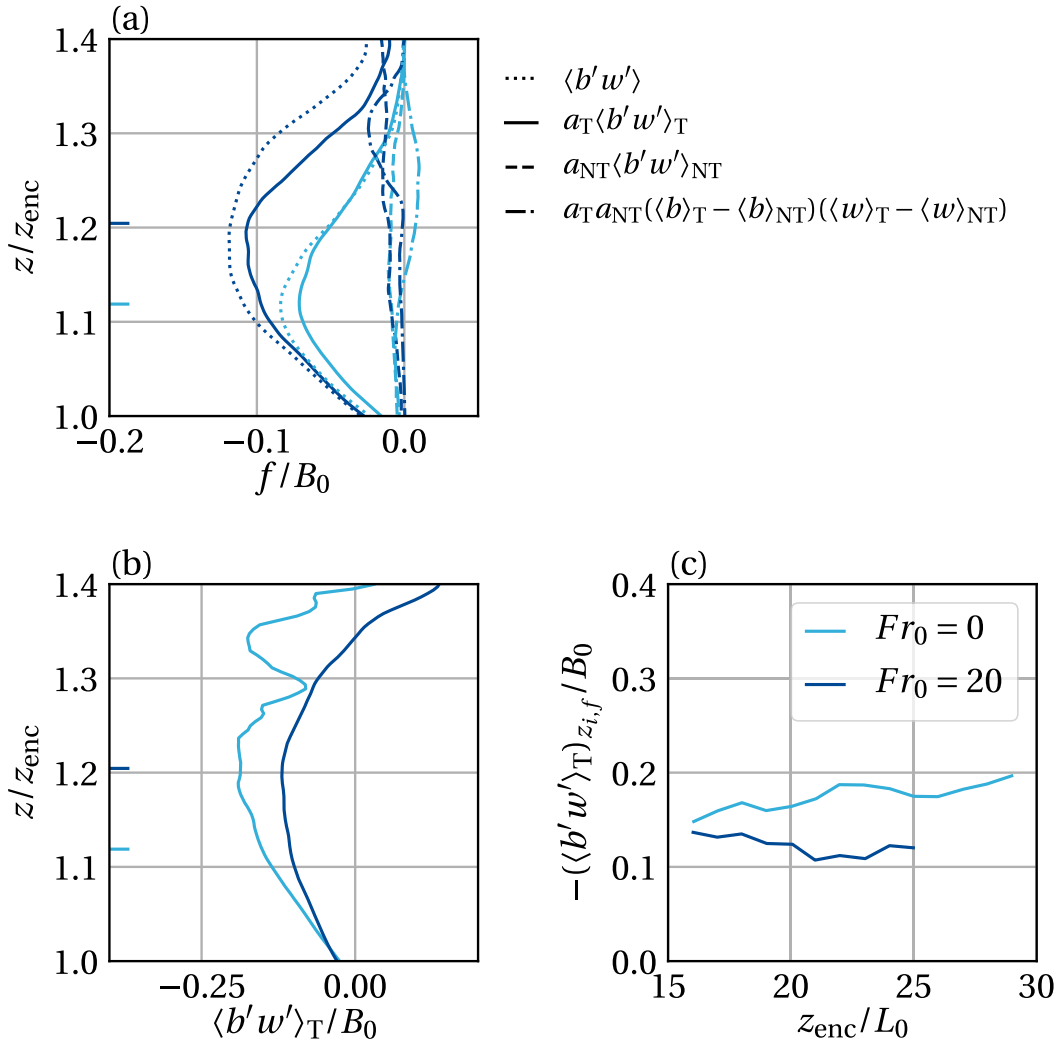
FIG. 6. (a) Contributions to the total buoyancy flux according to Eq. (1). The markers on the left-hand side indicate $z_{i,f}$. (b) Buoyancy flux within turbulent regions as a function of height at $z_{enc}/L_0 = 20$. (c) Entrainment flux ratio conditioned to turbulent regions as a function of time.

height in Fig. 6a for each Fr_0. It is immediately evident that the turbulent contribution is by far the largest to the total buoyancy flux and that wind shear does little to modify the other two terms. We can therefore already eliminate the first hypothesis posed in section 1 and write

$$\langle b'w' \rangle \approx a_T \langle b'w' \rangle_T. \tag{15}$$

We have seen that, in the sheared CBL, the turbulent area fraction at $z_{i,f}$ increases by around 70% of its shear-free value, whereas the increase in the magnitude of the total buoyancy flux at $z_{i,f}$ between $Fr_0 = 0$ and $Fr_0 = 20$ is around 50%. By Eq. (15), this suggests that $\langle b'w' \rangle_T$ should in fact become somewhat *smaller* with increasing Fr_0 and this is verified in Figs. 6b and 6c. Even with a lower enstrophy threshold in the shear-free case, the buoyancy

flux in turbulent regions remains similar to that in the sheared case, as shown in appendix A, which would seem to eliminate our second hypothesis that fluctuations become stronger in turbulent regions with increasing wind shear and thereby enhance the entrainment buoyancy flux. Although the first two hypotheses posed in section 1 were perhaps the more intuitive ones, our third hypothesis is confirmed: it is the increase in the turbulent area fraction with wind shear that is the main reason for the increase in the magnitude of the total buoyancy flux.

a. Why is the mean difference term so small?

It is not immediately obvious why our first hypothesis failed. In this section, we explore why the mean difference term turns out to be so small.
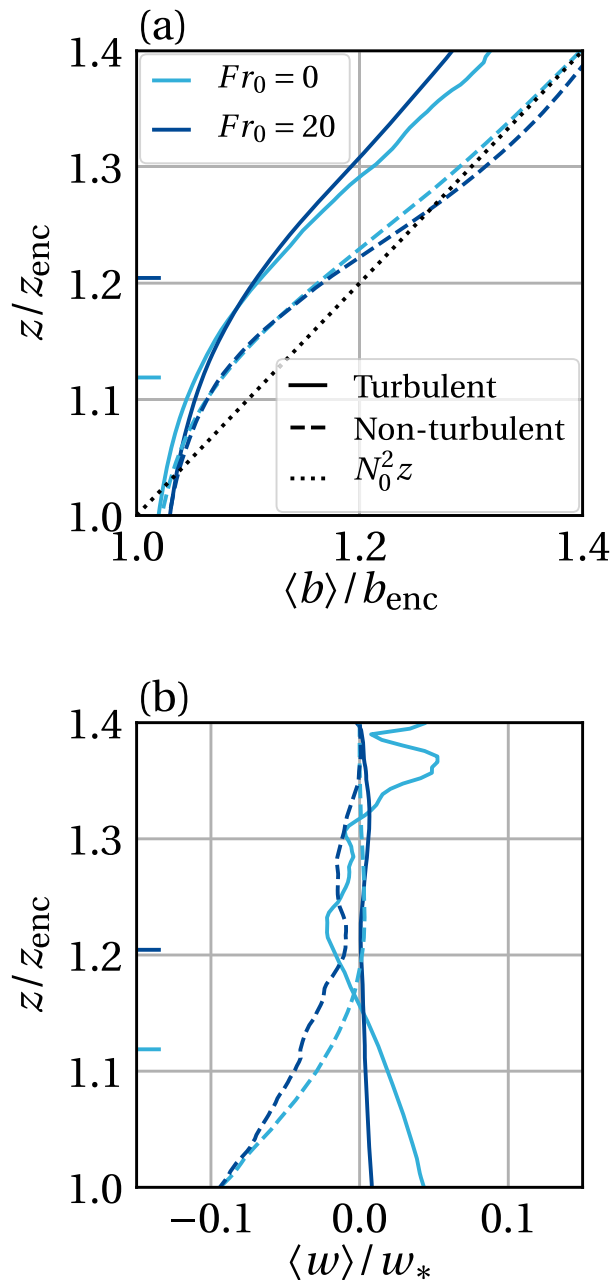
FIG. 7. (a) Mean buoyancy as a function of height and (b) mean vertical velocity as a function of height at $z_{enc}/L_0 = 20$. The scales b_{enc} and w_* are defined as $b_{enc} \equiv N_0^2 z_{enc}$ and $w_* \equiv (B_0 z_{enc})^{1/3}$. The markers on the left-hand side indicate $z_{i,f}$.

Figure 7 shows the mean buoyancy and the mean vertical velocity separately in turbulent and nonturbulent regions. The mean buoyancy in nonturbulent regions tends toward the background buoyancy profile $N_0^2 z$. The mean buoyancy in turbulent regions corresponds to air ascending from the mixed layer. As the turbulent thermals mix with their environment,

their mean buoyancy increases, resulting in a difference between $\langle b \rangle_T$ and $\langle b \rangle_{NT}$ of approximately $0.1 b_{enc}$ in the upper-entrainment-zone sublayer and free atmosphere ($b_{enc} \equiv N_0^2 z_{enc}$).

The mean vertical velocity in nonturbulent regions is negative in the lower-entrainment-zone sublayer due to entrained air moving down toward the boundary layer interior. Further up, $\langle w \rangle_{NT}$ becomes dominated by gravity wave motion, which, averaged over the horizontal plane, becomes zero. The mean vertical velocity in turbulent regions decreases to zero in the lower-entrainment-zone sublayer, which can be interpreted as a weakening of turbulent plumes as they penetrate into the overlying stratification. This effect is clearer in the shear-free CBL, as the vertical motion is stronger than in the sheared CBL. Fluctuations about zero in the upper-entrainment-zone sublayer and free atmosphere are due to limited statistical convergence as a_T becomes small.

Despite there being a relatively large difference between $\langle w \rangle_T$ and $\langle w \rangle_{NT}$ in the lower-entrainment-zone sublayer, the similarity between $\langle b \rangle_T$ and $\langle b \rangle_{NT}$ there results in a negligible contribution from the mean difference term in Eq. (1). In the upper-entrainment-zone sublayer, where the difference in the mean buoyancy between turbulent and nonturbulent regions increases, the mean velocity tends to zero in both regions and hence the mean difference term is also small there. This illustrates how nuanced the situation is, in that the mean buoyancy and mean vertical velocity *can* differ quite substantially between turbulent and nonturbulent regions, but the differences depend on height and precisely where there is a large difference in one variable between the two regions, it is cancelled out by an approximate equivalence between the two regions in the other variable.

b. Why does the buoyancy flux in turbulent regions not increase with wind shear?

We have seen that the turbulent contribution dominates the buoyancy flux, but that as wind shear increases, the magnitude of $\langle b'w' \rangle_T$ does not increase as one might expect from the increase in TKE. This leads us to examine more closely the second hypothesis posed in section 1 about whether wind shear generates more vigorous fluctuations within the turbulent region.

In Fig. 8, we show the buoyancy and vertical velocity root-mean-square (rms) conditioned to turbulent regions. Figures 8a and 8c show the vertical profiles. It can be seen that the buoyancy rms profiles in the shear-free and sheared cases lie on top of each other, whereas the
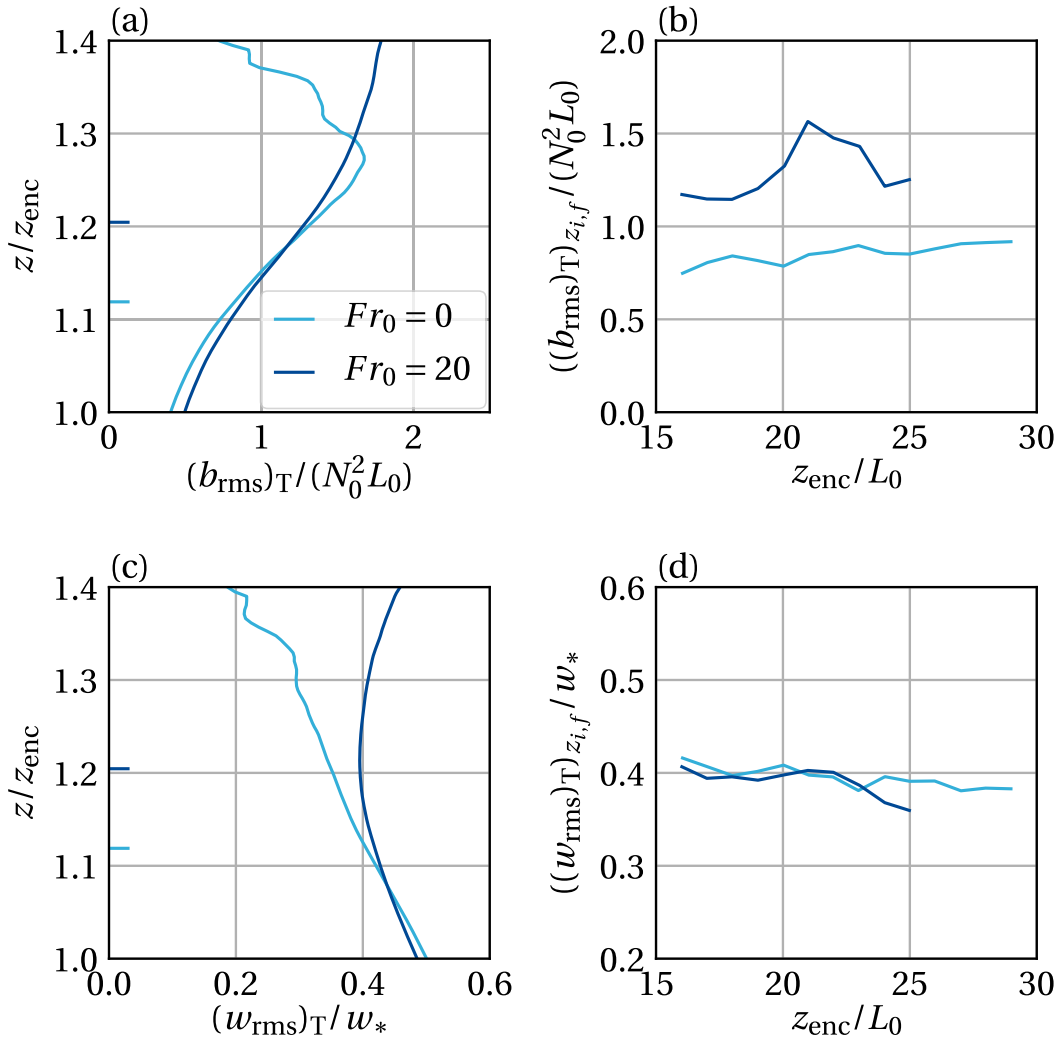
FIG. 8. (a),(b) Buoyancy rms and (c),(d) vertical velocity rms in turbulent regions as a function of (a),(c) height at $z_{enc}/L_0 = 20$ and (b),(d) time at $z_{i,f}$ for $Fr_0 = 0$ and $Fr_0 = 20$. The markers on the left-hand side in (a) and (c) indicate $z_{i,f}$.

vertical velocity rms profiles diverge from one another. However, when looking only at the height of minimum buoyancy flux (Figs. 8b,d), $(b_{rms})_T$ in the sheared CBL is at least 50% larger than in the shear-free CBL, while the vertical velocity rms in turbulent regions is hardly affected by wind shear. This behavior occurs because wind shear compounds two effects: first, the change in the vertical profile and second, the change in the height of $z_{i,f}$. On the one hand, $(b_{rms})_T$ increases with height in the entrainment zone, regardless of whether wind shear is present. But since $z_{i,f}$ moves higher up with shear, the buoyancy rms is larger at that reference height in the sheared CBL. On the other hand, $(w_{rms})_T$ decreases with height in the shear-free CBL, but curves back on itself in the sheared CBL. Hence the change in the profile and the change in the height of $z_{i,f}$ occur in such a way that they

effectively cancel out. This highlights the difficulty of ascertaining shear effects on entrainment-zone properties, as different effects can compensate each other.

It is perhaps surprising at first that the buoyancy flux within turbulent regions remains unchanged, or even weakens with wind shear (Figs. 6b,c), despite buoyancy fluctuations becoming stronger in turbulent regions at $z_{i,f}$ (Fig. 8b). However, as we have seen, vertical velocity fluctuations in turbulent regions at the same reference height do not increase with wind shear (Fig. 8d). This suggests that the two signals are not in phase with one another.

Kim et al. (2003) found that above $z_{i,f}$, temperature fluctuations tend to advance vertical velocity fluctuations with a phase difference of around $\pi/2$ and hence the buoyancy flux weakens, even though fluctuations are
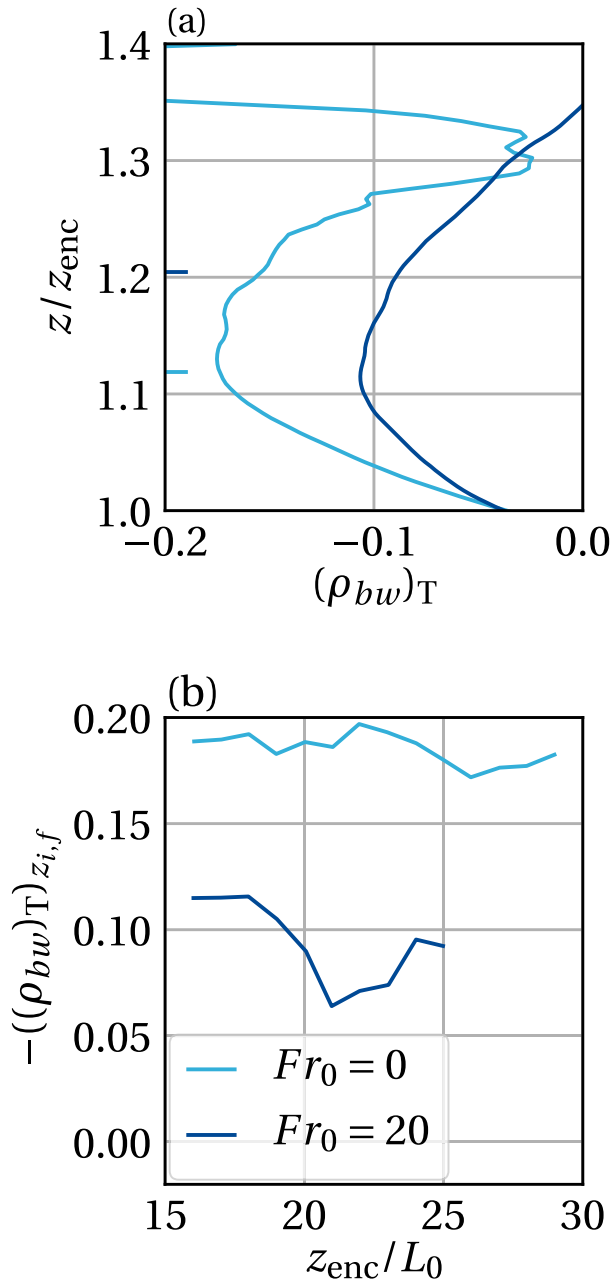
FIG. 9. Correlation between buoyancy and vertical velocity fluctuations in turbulent regions as a function of (a) height at $z_{enc}/L_0 = 20$ and (b) time at $z_{i,f}$. The markers on the left-hand side in (a) indicate $z_{i,f}$.

strong. We see here that when conditioned to turbulent patches, a phase difference must also exist at $z_{i,f}$. We quantify this by calculating the correlation coefficient between buoyancy and vertical velocity fluctuations within turbulent regions, as shown in Fig. 9. In the shear-free CBL, vertical velocity fluctuations are induced by buoyancy forces and there is a negative peak in the

correlation due to warmer air moving down and cooler air moving up. When wind shear is added to the system, buoyancy is no longer the only external source of vertical velocity fluctuations and the correlation consequently decreases.

By expressing the buoyancy flux in terms of the correlation coefficient,

$$\langle b'w'\rangle_T = (\rho_{bw})_T (b_{rms})_T (w_{rms})_T, \qquad (16)$$

it becomes clear that even though the buoyancy rms becomes stronger in turbulent regions at $z_{i,f}$, the decrease in the correlation coefficient compensates, or even overcompensates that increase, such that the buoyancy flux remains similar or weakens within turbulent regions under sheared conditions.

6. Summary and conclusions

The shear enhancement of the entrainment flux in the CBL is compounded by external intermittency: an alternation of turbulent (i.e., strongly vortical) and nonturbulent (i.e., weakly vortical) regions. Analysis tools employed in the past have not distinguished the various effects that wind shear can have on properties within these different regions. Here we have employed conditional analysis on direct numerical simulations of the shear-free and sheared CBL to investigate what this method can reveal about shear effects on entrainment that is otherwise hidden by conventional statistics.

We have shown that even with the moderate Reynolds numbers we are able to achieve in our simulations, a clear distinction between turbulent and nonturbulent regions is possible. Peaks in the probability density function of enstrophy representing the turbulent boundary layer and the nonturbulent free atmosphere are separated by two orders of magnitude. As shown in appendix C, this scale separation increases only marginally when considering the potential vorticity, and low values of the potential vorticity inside the mixed layer, leading to a small mixed-layer turbulent area fraction, ultimately led us to favor enstrophy as a conditioning variable. Nonetheless, the results and conclusions are robust, both with respect to the two conditioning variables, and within the two-decade range of enstrophy thresholds considered in our analysis.

As a first application, we have demonstrated the utility of this kind of conditioning for understanding shear effects on entrainment. We have found that the largest contribution to the entrainment flux ratio, $-\langle b'w'\rangle_{z_{i,f}}/B_0$, comes from turbulent regions and not

from the difference in mean properties between turbulent and nonturbulent regions. Yet the main reason that the entrainment flux ratio increases with wind shear is *not* because the flux itself becomes stronger in turbulent regions, despite what might be expected from the increase in turbulent kinetic energy. Although buoyancy fluctuations do become stronger under sheared conditions, there is a compensating effect due to the decrease in the correlation between buoyancy and vertical velocity fluctuations. Hence, the main reason the entrainment flux increases with wind shear is simply due to there being a larger turbulent area in which entrainment can take place more efficiently than in nonturbulent regions.

In light of these results, it would be interesting to reconsider the case of weak shear conditions in a future study, where the entrainment buoyancy flux initially reduces compared to the shear-free case. It is thought that this is due to the redistribution of the kinetic energy of thermals to horizontal velocity fluctuations (Fedorovich et al. 2001). Given our findings though, an alternative possibility is that weak shear reduces the correlation between buoyancy and vertical velocity fluctuations more than it increases the turbulent area fraction. These two hypotheses could be examined and compared through a conditional analysis of the Reynolds stress transport equation.

The importance of the turbulent area fraction for governing changes in conventional statistics was also identified by Ansorge and Mellado (2016) for the stably stratified Ekman layer. As originally proposed by those authors, this suggests a novel approach to the parameterization of fluxes within the atmospheric boundary layer. We have seen that in the entrainment zone of the CBL, vertical fluxes can be approximated as $\langle \phi' \omega' \rangle \approx a_T \langle \phi' \omega' \rangle_T$. A standard method could then be used for modeling the flux within turbulent regions, while the turbulent area fraction could be expressed as a function of z/z_{enc} and Fr_0. This idea is similar in design to mass-flux approaches used for the parameterization of cumulus convection, where the cloud core area fraction is modeled as a function of the specific humidity (Neggers et al. 2006). In this regard, it would also be interesting to apply the conditioning procedure presented here to properties such as the humidity and temperature variance, which are key to understand and model cloud formation, but their dependence on environmental conditions in the entrainment zone is difficult to ascertain (Mellado et al. 2017).

The potential applications of this kind of conditional analysis need not be restricted to the dry CBL. Cloud boundaries coexist with the turbulent/nonturbulent interface, but do not normally coincide (Moeng et al. 2005; Mellado 2017). While conditioning on the liquid water content to distinguish between cloudy and noncloudy air has been used in the past to study various aspects of cloud mass transport, entrainment and detrainment (de Roode and Wang 2007; Jonker 2008), further useful insights may well be gained by conditioning statistics into turbulent and nonturbulent regions. For instance, when the cloud boundary is well inside the turbulent region instead of close to the turbulent–nonturbulent interface, the properties of the turbulent fluctuations might be closer to those of homogeneous turbulence, which would facilitate its modeling.

APPENDIX A

Dependence on Enstrophy Threshold

To ascertain to what extent our results regarding wind shear effects on the buoyancy flux, the buoyancy rms and the vertical velocity rms depend on the threshold chosen to distinguish turbulent from nonturbulent regions, we examine these properties as a function of threshold.

Figures A1a and A1b show the conditioned buoyancy flux at $z_{i,f}$. As explained in section 4, nonturbulent statistics (left column of Fig. A1) in the limit of increasing thresholds converge with turbulent statistics (right column of Fig. A1) in the limit of decreasing thresholds and this converged profile is equivalent to the conventional statistic. Within the range of thresholds $-1.5 \lesssim \log_{10}(\omega_{th}^2/\omega_0^2) \lesssim 0.5$ given in section 4, where $0.1 \lesssim (a_T)_{z_{i,f}} \lesssim 0.9$ in the shear-free case and the conditioning may be considered meaningful, $\langle b'w' \rangle_T$ at $z_{i,f}$ is similar, or smaller at $Fr_0 = 20$ compared to $Fr_0 = 0$. Hence this result is not an outcome of the specific threshold we chose.
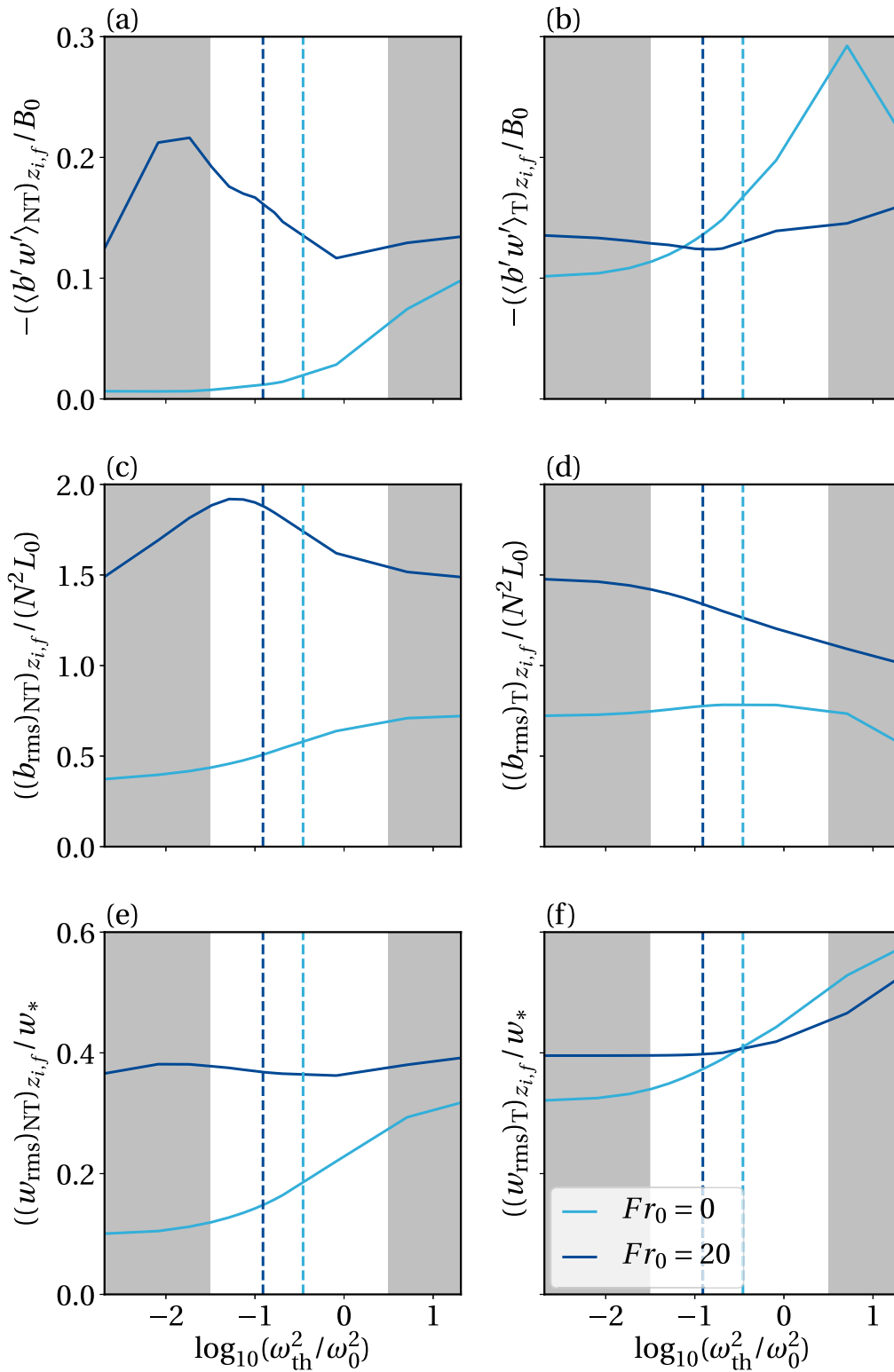
FIG. A1. (a),(b) Buoyancy flux, (c),(d) buoyancy rms, and (e),(f) vertical velocity rms at $z_{i,f}$ conditioned to (a),(c),(e) nonturbulent and (b),(d),(f) turbulent regions as a function of enstrophy threshold at $z_{enc}/L_0 = 20$. The dashed lines indicate the reference threshold defined in section 3. The gray shaded areas indicate the range of thresholds where the turbulent area fraction in the shear-free case is greater than 0.9 or less than 0.1.

Figures A1c and A1d demonstrate that the increase of the buoyancy rms with wind shear is also independent of the specific threshold chosen. Both $(b_{rms})_T$ and $(b_{rms})_{NT}$ are larger at $z_{i,f}$ in the $Fr_0 = 20$ case across the full range of thresholds considered. Figures A1e and A1f show that $(w_{rms})_T$ at $z_{i,f}$ remains similar between $Fr_0 = 0$ and $Fr_0 = 20$ for a comparable threshold within the range $-1.5 \lesssim \log_{10}(\omega_{th}^2/\omega_0^2) \lesssim 0.5$.

APPENDIX B

Reynolds Number Dependence

Since we are restricted to low to moderate Reynolds numbers, it is worthwhile to consider the extent to which changes to the Reynolds number influence our results. Reynolds number effects are strongest for the shear-free CBL so in this section, we only show results relating to $Fr_0 = 0$.

As expected, Fig. B1 indicates that the scale separation between the boundary layer and free atmosphere increases with Reynolds number. The scale ω_0^2 characterizes the enstrophy in the mixed layer for all Reynolds numbers considered and as the Reynolds number is increased, the characteristic vorticity magnitudes in the free atmosphere decrease in comparison, as seen by a shift in the upper lobes of the PDFs toward smaller normalized enstrophy values. Correspondingly, the saddle point also moves to smaller enstrophy values.

The change in the PDFs with increasing Reynolds number is also reflected by the turbulent area fraction in Fig. B2. Contours indicating a nonzero turbulent area fraction in the free atmosphere show a marked shift toward lower normalized enstrophy values as Re_0 increases from 25 to 117. The contours within the upper-entrainment-zone sublayer (i.e., around the height $z_{i,g}$) consequently flatten. This suggests that at the very high Reynolds numbers that characterize the real CBL, the turbulent area fraction would become very insensitive to the threshold in the upper-entrainment-zone sublayer.

APPENDIX C

Potential Enstrophy as a Conditioning Variable

Because gravity waves possess vorticity, this reduces the scale separation between the turbulent boundary layer and the nonturbulent free stream compared to nonstratified flows. One way this problem could be countered is to use potential enstrophy, rather than enstrophy, as a turbulence indicator (Riley and Lelong
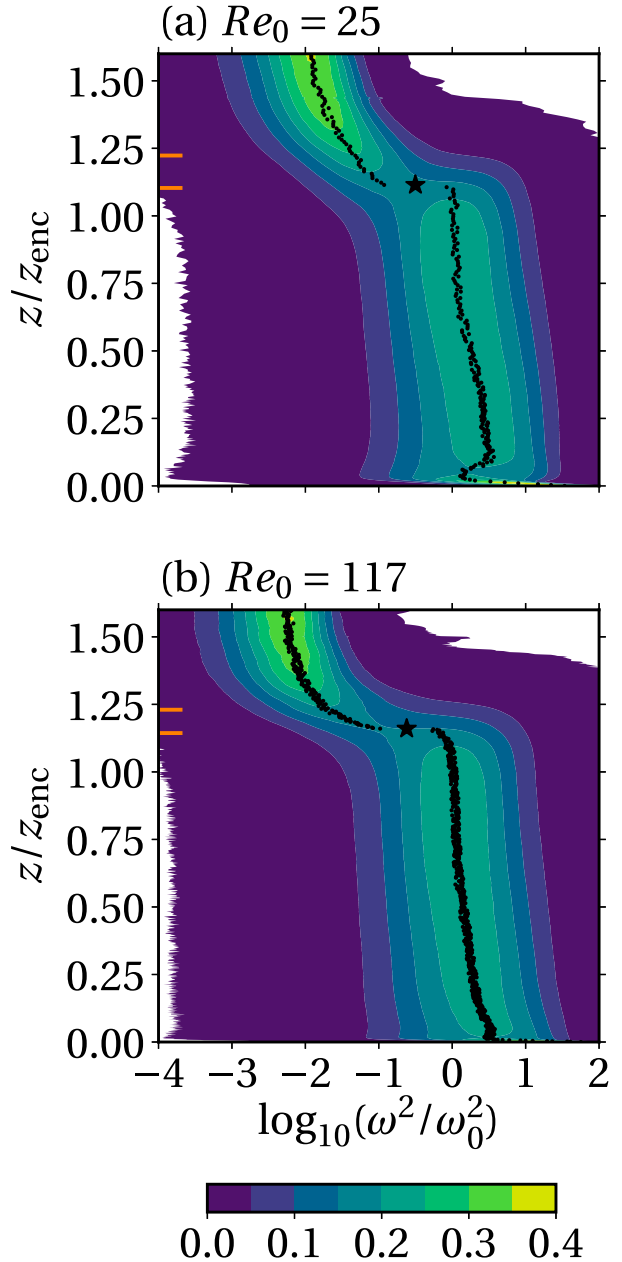

FIG. B1. Probability distribution functions of enstrophy at $z_{enc}/L_0 = 20$. The black dots indicate the mode of the PDF at each height. The star shows the approximate saddle point. The lower and upper orange markers on the left-hand side indicate $z_{i,f}$ and $z_{i,g}$, respectively. The reference scale ω_0^2 is defined in Eq. (14) with $c_\varepsilon = 0.1$.

2000; Watanabe et al. 2016). Here we assess the suitability of potential enstrophy as a turbulence indicator in the CBL and verify the robustness of our results with respect to this alternative conditioning variable.

The potential vorticity is defined as $\Pi \equiv \boldsymbol{\omega} \cdot \nabla b$. We therefore require an estimate of the magnitude of the buoyancy gradient in the mixed layer to provide a
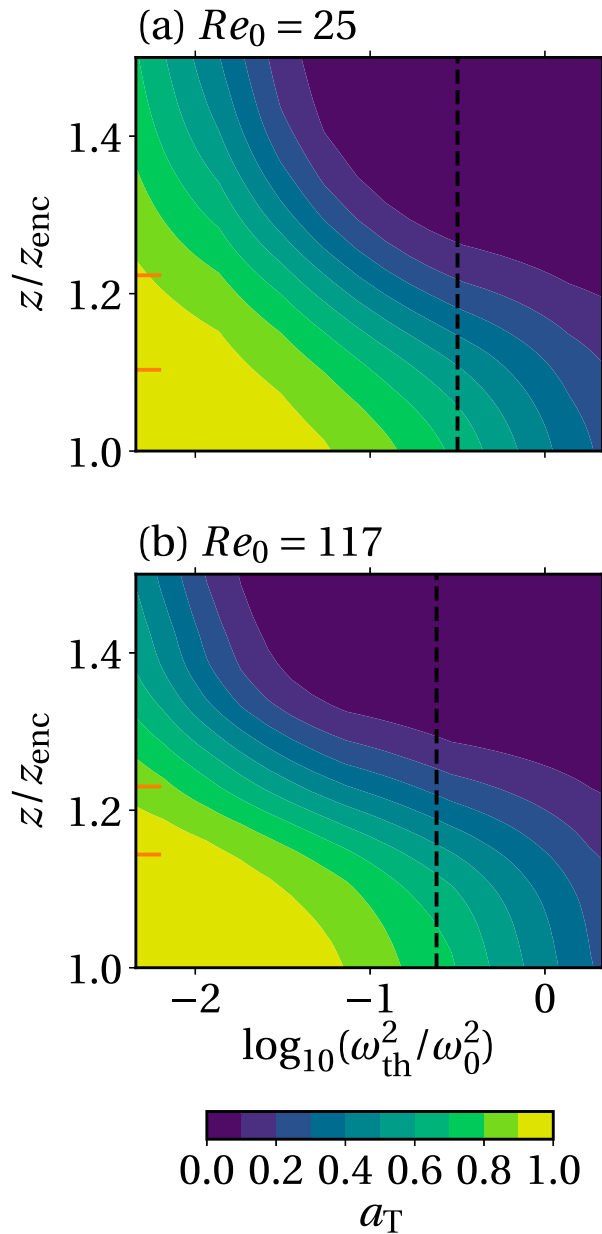
FIG. B2. Turbulent area fraction as a function of height and enstrophy threshold at $z_{enc}/L_0 = 20$. The black dashed line indicates the magnitude at which the saddle point in Fig. B1 is located. The lower and upper orange markers on the left-hand side indicate $z_{i,f}$ and $z_{i,g}$, respectively.

reference scale for Π. We start by estimating the buoyancy variance dissipation rate as

$$\kappa \langle |\nabla b'|^2 \rangle \sim \frac{b_{rms}^2}{z_{enc}/w_{rms}}, \qquad (C1)$$

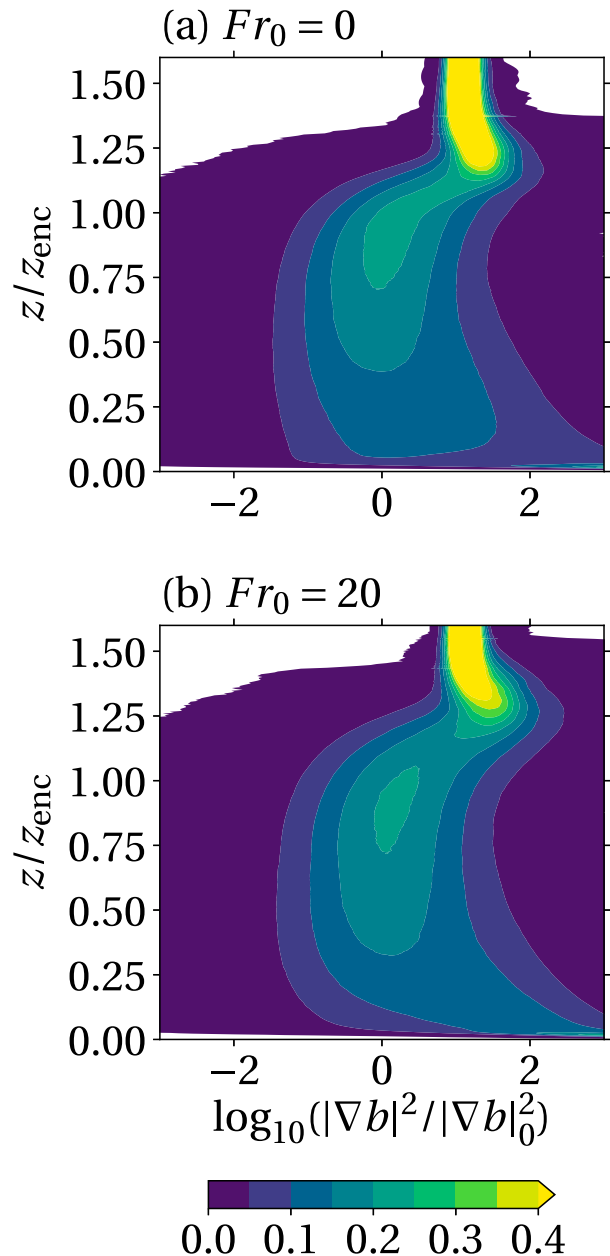where z_{enc}/w_{rms} is the eddy turnover time. Our Eq. (C1) follows the scaling arguments of Wyngaard (2010)

FIG. C1. Probability density functions of the buoyancy gradient at $z_{enc}/L_0 = 20$. The reference scale $|\nabla b|_0$ is defined in Eq. (C2) with $c_b = 0.1$.

and is analogous to their Eq. (5.21). Then, by estimating $b_{rms} \sim B_0/w_{rms}$ and $w_{rms} \sim (z_{enc}B_0)^{1/3}$ and using the definitions of L_0 [Eq. (5)], $\nu/\kappa \equiv 1$, and Re_0 [Eq. (3)], one finds a reference buoyancy gradient scale in the mixed layer as

$$|\nabla b| \equiv c_b N_0^4 Re_0 \left(\frac{z_{enc}}{L_0} \right)^{-4/3}. \qquad (C2)$$

This reference scale is verified with $c_b = 0.1$ in Fig. C1.

From the definition of Π, Eq. (14), and Eq. (C2), the reference scale for potential enstrophy in the mixed layer is

$$\Pi_0^2 \equiv c_b c_\epsilon N_0^6 \text{Re}_0^2 \left(\frac{z_{\text{enc}}}{L_0}\right)^{-4/3}. \qquad (\text{C3})$$

It should be noted that since $\boldsymbol{\omega} \cdot \nabla b = |\boldsymbol{\omega}||\nabla b|\cos\alpha$, where α is the angle between the two vectors, the product of ω_0 and $|\nabla b|_0$ will overestimate the magnitude of the potential vorticity in the mixed layer if the vorticity and buoyancy gradient vectors are not well aligned. Figure C2 indicates that Π_0^2 indeed overestimates the potential enstrophy in the mixed layer by about two orders of magnitude, suggesting that the vorticity and buoyancy gradient vectors are far from parallel. This was verified by checking the cosine of the angle between the two vectors, which was found to be close to zero everywhere (not shown). Hence, the vorticity and buoyancy gradient vectors are approximately perpendicular, as also shown by Kerr (1985) and Ashurst et al. (1987) for the vorticity and passive scalar gradient.

Since potential vorticity cannot be propagated by gravity waves, the only way the free atmosphere can obtain potential vorticity in our simulations is through diffusion. Due to restrictions on the Reynolds number, viscous and diffusive effects are much stronger in our simulations than they would be in the real atmosphere. Diffusive effects do diminish away from the boundary layer, as may be seen from the decreasing potential enstrophy values of the mode of the PDF in the free atmosphere in Fig. C2, but still, it is clear that little has been gained in terms of scale separation compared to using enstrophy.

We use the same method for approximating the saddle point as described before, the jump size between consecutive grid levels being a factor of roughly $1.5\Pi^2/\Pi_0^2$ in the $\text{Fr}_0 = 0$ case and a factor of roughly $5\Pi^2/\Pi_0^2$ in the $\text{Fr}_0 = 20$ case. The mean value of the saddle point over time is used as the threshold on potential enstrophy for distinguishing between turbulent and nonturbulent regions. Using this method, the turbulent area fraction is shown in Fig. C3. The vertical profile indicates that there is a smaller turbulent area fraction within the mixed layer than inside the lower-entrainment-zone sublayer. This unintuitive outcome is due to the behavior of the buoyancy gradient in the CBL, which strongly affects the magnitude of the potential vorticity. Because the buoyancy gradient increases sharply from the mixed layer to the entrainment zone, the potential enstrophy follows suit (see also Fig. C2). This means that for a given threshold, there is a larger area where the potential enstrophy is
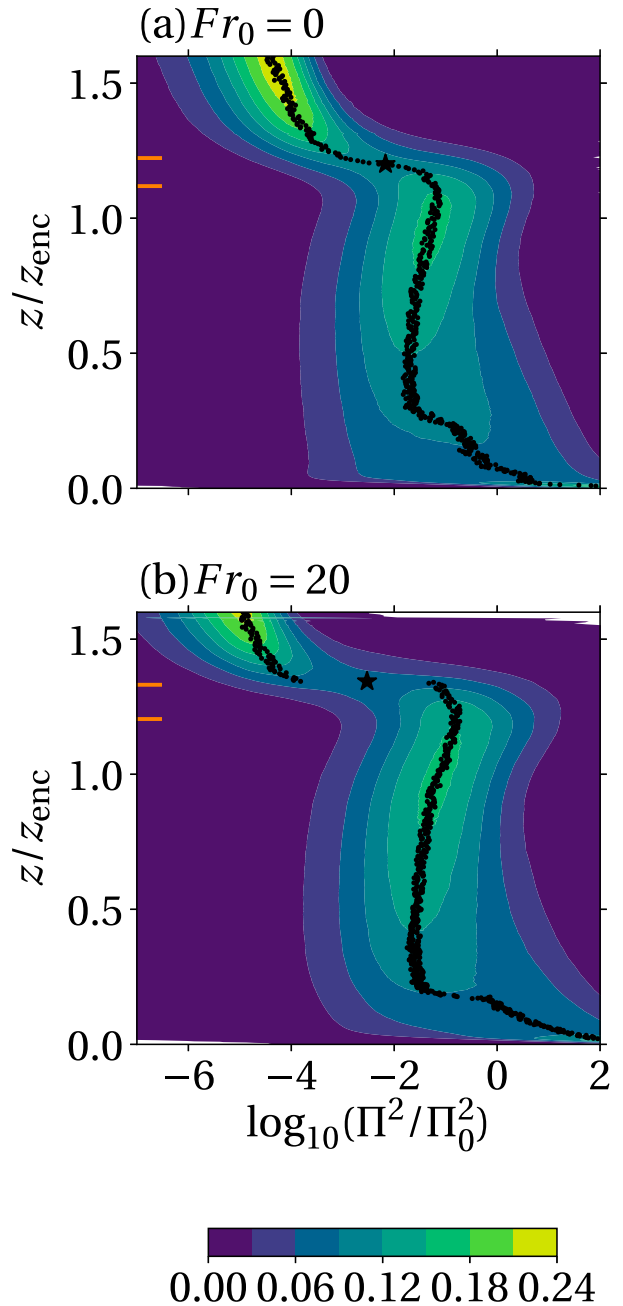

FIG. C2. Probability density functions of potential enstrophy at $z_{\text{enc}}/L_0 = 20$. The black dots indicate the mode of the PDF at each height. The star shows the approximate saddle point. The lower and upper orange markers on the left-hand side indicate $z_{i,f}$ and $z_{i,g}$, respectively. The reference scale Π_0 is defined in Eq. (C3) with $c_b = c_\varepsilon = 0.1$.

greater than the threshold in the entrainment zone and hence why there is a bigger turbulent area fraction there than in the mixed layer. For this reason, the potential enstrophy is somewhat less suitable than the enstrophy as a turbulence indicator in the CBL.
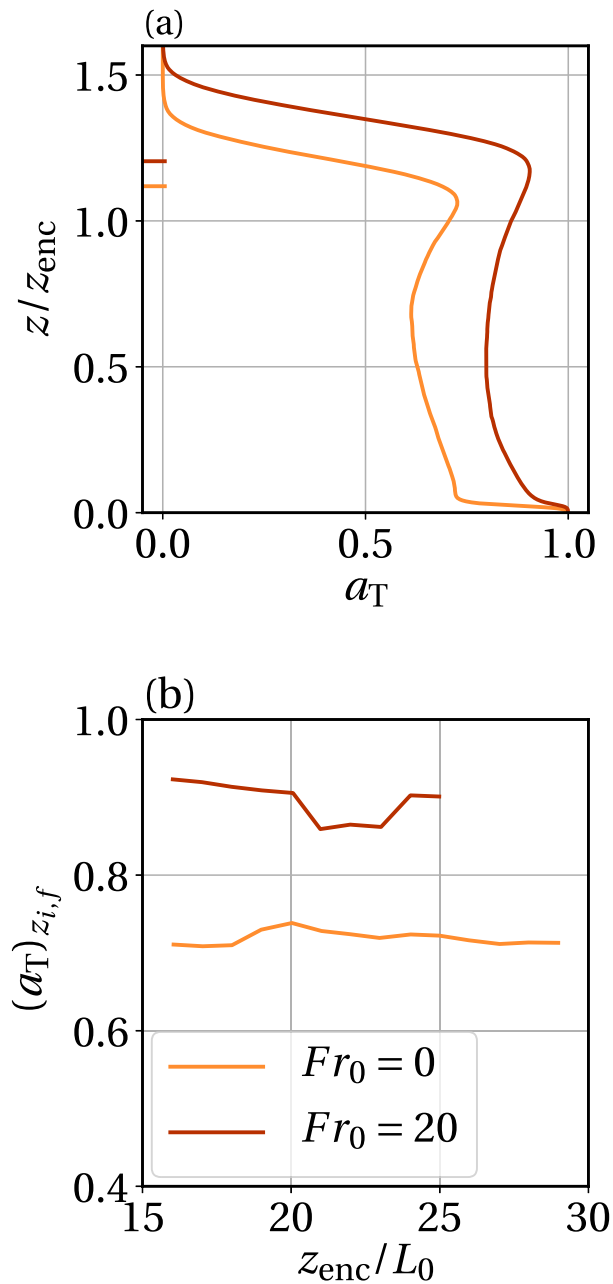
FIG. C3. Turbulent area fraction as a function of (a) height at $z_{enc}/L_0 = 20$ and (b) time at $z_{i,f}$. The threshold used in each case is the mean value of the saddle point in the potential enstrophy PDF between $15 \leq z_{enc}/L_0 \leq 30$. The markers on the left-hand side in (a) indicate $z_{i,f}$.
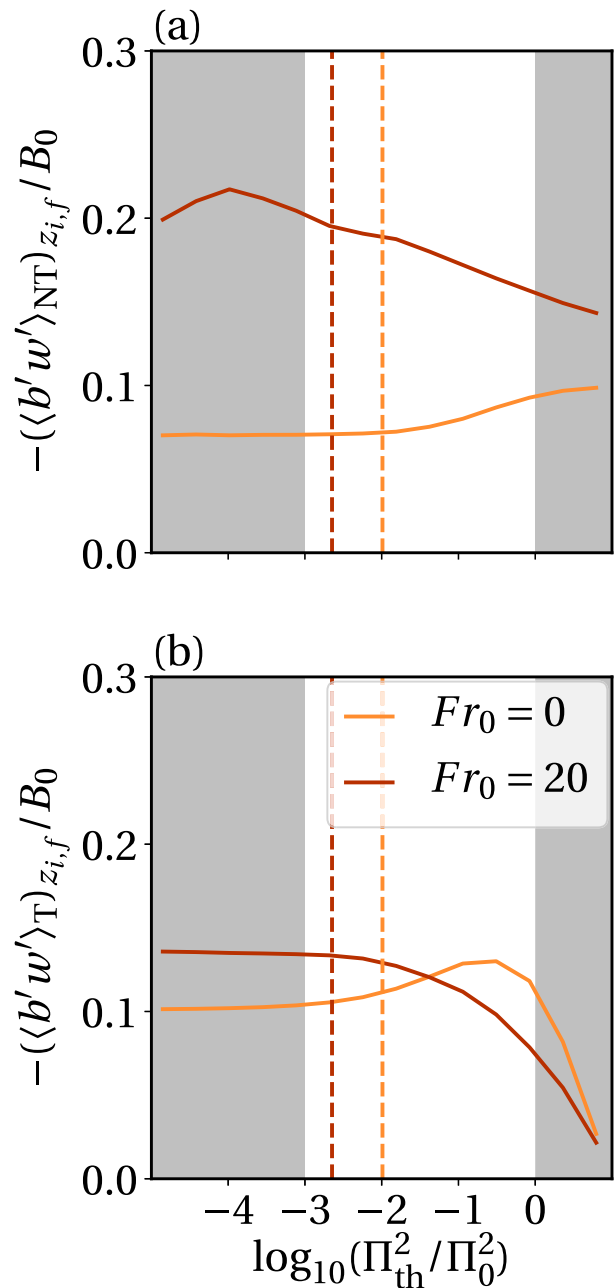
FIG. C4. Buoyancy flux at $z_{i,f}$ conditioned to (a) nonturbulent and (b) turbulent regions as a function of potential enstrophy threshold at $z_{enc}/L_0 = 20$. The dashed lines indicate the reference threshold. The gray shaded areas indicate the range of thresholds where the turbulent area fraction in the shear-free case is greater than 0.9 or less than 0.1.

Nevertheless, we can still assess how robust our results are using the potential enstrophy as a conditioning variable. With our reference threshold, the increase in the turbulent area fraction at $Fr_0 = 20$ is around 30% of the shear-free value (Fig. C3), while the increase in the total buoyancy flux is around 50%. Hence, there is a contribution of around 20% that is not explained by the

increase in the turbulent area fraction. In Fig. C4, we show the buoyancy flux at $z_{i,f}$ over a range of potential enstrophy thresholds. As in Fig. A1, we have greyed out threshold ranges where, in the shear-free case, $(a_T)_{z_{i,f}} > 0.9$ and $(a_T)_{z_{i,f}} < 0.1$. Within the range of

physically meaningful thresholds, the buoyancy flux in turbulent regions varies by no more than 20% between the shear-free and sheared cases. This explains the additional contributing factor, but also shows that the turbulent area fraction is still the leading order parameter in the shear enhancement of the entrainment flux and thus the main conclusions of this paper are robust with respect to the conditioning variable.

REFERENCES

Ansorge, C., and J.-P. Mellado, 2016: Analyses of external and global intermittency in the logarithmic layer of Ekman flow. *J. Fluid Mech.*, **805**, 611–635, https://doi.org/10.1017/jfm.2016.534.

Antonia, R., 1981: Conditional sampling in turbulence measurement. *Annu. Rev. Fluid Mech.*, **13**, 131–156, https://doi.org/10.1146/annurev.fl.13.010181.001023.

Ashurst, W., A. Kerstein, R. Kerr, and C. Gibson, 1987: Alignment of vorticity and scalar gradient with strain rate in simulated Navier-Stokes turbulence. *Phys. Fluids*, **30**, 2343–2353, https://doi.org/10.1063/1.866513.

Bisset, D., J. Hunt, and M. Rogers, 2002: The turbulent/non-turbulent interface bounding a far wake. *J. Fluid Mech.*, **451**, 383–410, https://doi.org/10.1017/S0022112001006759.

Borrell, G., and J. Jiménez, 2016: Properties of the turbulent/non-turbulent interface in boundary layers. *J. Fluid Mech.*, **801**, 554–596, https://doi.org/10.1017/jfm.2016.430.

Conzemius, R., and E. Fedorovich, 2006: Dynamics of sheared convective boundary layer entrainment. Part I: Methodological background and large-eddy simulations. *J. Atmos. Sci.*, **63**, 1151–1178, https://doi.org/10.1175/JAS3691.1.

Corrsin, S., and A. Kistler, 1955: Free-stream boundaries of turbulent flows. National Advisory Committee on Aeronautics Tech. Rep. 1244, 32 pp.

da Silva, C., J. Hunt, I. Eames, and J. Westerweel, 2014a: Interfacial layers between regions of different turbulence intensity. *Annu. Rev. Fluid Mech.*, **46**, 567–590, https://doi.org/10.1146/annurev-fluid-010313-141357.

——, R. Taveira, and G. Borrell, 2014b: Characteristics of the turbulent/non-turbulent interface in boundary layers, jets and shear-free turbulence. *J. Phys. Conf. Ser.*, **506**, 012015, https://doi.org/10.1088/1742-6596/506/1/012015.

Deardorff, J., 1970: Convective velocity and temperature scales for the unstable planetary boundary layer and for Rayleigh convection. *J. Atmos. Sci.*, **27**, 1211–1213, https://doi.org/10.1175/1520-0469(1970)027<1211:CVATSF>2.0.CO;2.

——, G. Willis, and B. Stockton, 1980: Laboratory studies of the entrainment zone of a convectively mixed layer. *J. Fluid Mech.*, **100**, 41–64, https://doi.org/10.1017/S0022112080001000.

de Roode, S. R., and Q. Wang, 2007: Do stratocumulus clouds detrain? FIRE I data revisited. *Bound.-Layer Meteor.*, **122**, 479–491, https://doi.org/10.1007/s10546-006-9113-1.

Dopazo, C., 1977: On conditioned averages for intermittent turbulent flows. *J. Fluid Mech.*, **81**, 433–438, https://doi.org/10.1017/S0022112077002158.

Dougherty, J., 1961: The anisotropy of turbulence at the meteor level. *J. Atmos. Terr. Phys.*, **21**, 210–213, https://doi.org/10.1016/0021-9169(61)90116-7.

Fedorovich, E., and R. Conzemius, 2008: Effects of wind shear on the atmospheric convective boundary layer structure and evolution. *Acta Geophys.*, **56**, 114–141, https://doi.org/10.2478/s11600-007-0040-4.

——, F. Niuewstadt, and R. Kaiser, 2001: Numerical and laboratory study of horizontally evolving convective boundary layer. Part II: Effects of elevated wind shear and surface roughness. *J. Atmos. Sci.*, **58**, 546–560, https://doi.org/10.1175/1520-0469(2001)058<0546:NALSOH>2.0.CO;2.

——, R. Conzemius, and D. Mironov, 2004: Convective entrainment into a shear-free, linearly stratified atmosphere: Bulk models reevaluated through large eddy simulations. *J. Atmos. Sci.*, **61**, 281–295, https://doi.org/10.1175/1520-0469(2004)061<0281:CEIASL>2.0.CO;2.

Fodor, K., J.-P. Mellado, and M. Wilczek, 2019: On the role of large-scale updrafts and downdrafts in deviations from Monin–Obukhov similarity theory in free convection. *Bound.-Layer Meteor.*, **172**, 371–396, https://doi.org/10.1007/s10546-019-00454-3.

Garcia, J., and J.-P. Mellado, 2014: The two-layer structure of the entrainment zone in the convective boundary layer. *J. Atmos. Sci.*, **71**, 1935–1955, https://doi.org/10.1175/JAS-D-13-0148.1.

Haghshenas, A., and J.-P. Mellado, 2019: Characterization of wind-shear effects on entrainment in a convective boundary layer. *J. Fluid Mech.*, **858**, 145–183, https://doi.org/10.1017/jfm.2018.761.

Holzner, M., and M. van Reeuwijk, 2017: The turbulent/non-turbulent interface in penetrative convection. *J. Turbul.*, **18**, 260–270, https://doi.org/10.1080/14685248.2016.1275655.

Hunt, J., and P. Durbin, 1999: Perturbed vortical layers and shear sheltering. *Fluid Dyn. Res.*, **24**, 375–404, https://doi.org/10.1016/S0169-5983(99)00009-X.

Jonker, H., 2008: A refined view of vertical mass transport by cumulus convection. *Geophys. Res. Lett.*, **35**, L07810, https://doi.org/10.1029/2007GL032606.

——, M. van Reeuwijk, P. Sullivan, and E. Patton, 2013: On the scaling of shear-driven entrainment: A DNS study. *J. Fluid Mech.*, **732**, 150–165, https://doi.org/10.1017/jfm.2013.394.

Kerr, R., 1985: Higher-order derivative correlations and the alignment of small-scale structures in isotropic numerical turbulence. *J. Fluid Mech.*, **153**, 31–58, https://doi.org/10.1017/S0022112085001136.

Khanna, S., and J. Brasseur, 1998: Three-dimensional buoyancy- and shear-induced local structure of the atmospheric boundary layer. *J. Atmos. Sci.*, **55**, 710–743, https://doi.org/10.1175/1520-0469(1998)055<0710:TDBASI>2.0.CO;2.

Kim, S.-W., S.-U. Park, and C.-H. Moeng, 2003: Entrainment processes in the convective boundary layer with varying wind shear. *Bound.-Layer Meteor.*, **108**, 221–245, https://doi.org/10.1023/A:1024170229293.

Kovasznay, L., V. Kibens, and R. Blackwelder, 1970: Large-scale motion in the intermittent region of a turbulent boundary layer. *J. Fluid Mech.*, **41**, 283–325, https://doi.org/10.1017/S0022112070000629.

LeMone, M., 1973: The structure and dynamics of horizontal roll vortices in the planetary boundary layer. *J. Atmos. Sci.*, **30**, 1077–1091, https://doi.org/10.1175/1520-0469(1973)030<1077:TSADOH>2.0.CO;2.

——, and Coauthors, 2019: 100 years of progress in boundary layer meteorology. *A Century of Progress in Atmospheric and Related Sciences: Celebrating the American Meteorological Society Centennial*, Meteor. Monogr., No. 59, Amer. Meteor. Soc, https://doi.org/10.1175/AMSMONOGRAPHS-D-18-0013.1.

Lohou, F., F. Saïd, M. Lothon, P. Durand, and D. Serça, 2010: Impact of boundary-layer processes on near-surface turbulence within

the west African monsoon. *Bound.-Layer Meteor.*, **136**, 1–23, https://doi.org/10.1007/s10546-010-9493-0.

Mellado, J.-P., 2017: Cloud-top entrainment in stratocumulus clouds. *Annu. Rev. Fluid Mech.*, **49**, 145–169, https://doi.org/10.1146/annurev-fluid-010816-060231.

——, L. Wang, and N. Peters, 2009: Gradient trajectory analysis of a scalar field with external intermittency. *J. Fluid Mech.*, **626**, 333–365, https://doi.org/10.1017/S0022112009005886.

——, M. Puche, and C. van Heerwaarden, 2017: Moisture statistics in free convective boundary layers growing into linearly stratified atmospheres. *Quart. J. Roy. Meteor. Soc.*, **143**, 2403–2419, https://doi.org/10.1002/qj.3095.

——, C. Bretherton, B. Stevens, and M. Wyant, 2018: DNS and LES for simulating stratocumulus: Better together. *J. Adv. Model. Earth Syst.*, **10**, 1421–1438, https://doi.org/10.1029/2018MS001312.

Moeng, C.-H., B. Stevens, and P. Sullivan, 2005: Where is the interface of the stratocumulus-topped PBL? *J. Atmos. Sci.*, **62**, 2626–2631, https://doi.org/10.1175/JAS3470.1.

Neggers, R., B. Stevens, and J. Neelin, 2006: A simple equilibrium model for shallow-cumulus-topped mixed layers. *Theor. Comput. Fluid Dyn.*, **20**, 305–322, https://doi.org/10.1007/s00162-006-0030-1.

Ozmidov, R., 1965: On the turbulent exchange in a stably stratified ocean. *Izv. Acad. Sci. USSR, Atmos. Oceanic Phys.*, **1**, 853–860.

Pino, D., and J. V.-G. de Arrellano, 2008: Effects of shear in the convective boundary layer: Analysis of the turbulent kinetic energy budget. *Acta Geophys.*, **56**, 167–193, https://doi.org/10.2478/s11600-007-0037-z.

——, ——, and P. Duynkerke, 2003: The contribution of shear to the evolution of a convective boundary layer. *J. Atmos. Sci.*, **60**, 1913–1926, https://doi.org/10.1175/1520-0469(2003)060<1913:TCOSTT>2.0.CO;2.

Pope, S., 2001: *Turbulent Flows*. Cambridge University Press, 771 pp.

Riley, J., and M.-P. Lelong, 2000: Fluid motions in the presence of strong stable stratification. *Annu. Rev. Fluid Mech.*, **32**, 613–657, https://doi.org/10.1146/annurev.fluid.32.1.613.

Salesky, S., M. Chamecki, and E. Bou-Zeid, 2017: On the nature of the transition between roll and cellular organization in the convective boundary layer. *Bound.-Layer Meteor.*, **163**, 41–68, https://doi.org/10.1007/s10546-016-0220-3.

Siebesma, A., P. Soares, and J. Teixeira, 2007: A combined eddy-diffusivity mass-flux approach for the convective boundary layer. *J. Atmos. Sci.*, **64**, 1230–1248, https://doi.org/10.1175/JAS3888.1.

Stull, R., 1988: *An Introduction to Boundary Layer Meteorology*. Kluwer Academic Publishers, 670 pp.

Sullivan, P., C.-H. Moeng, B. Stevens, D. Lenschow, and S. Mayor, 1998: Structure of the entrainment zone capping the convective atmospheric boundary layer. *J. Atmos. Sci.*, **55**, 3042–3064, https://doi.org/10.1175/1520-0469(1998)055<3042:SOTEZC>2.0.CO;2.

van de Boer, A., A. F. Moene, A. Graf, D. Schüttemeyer, and C. Simmer, 2014: Detection of entrainment influences on surface-layer measurements and extension of Monin–Obukhov similarity theory. *Bound.-Layer Meteor.*, **152**, 19–44, https://doi.org/10.1007/s10546-014-9920-8.

van Reeuwijk, M., and M. Holzner, 2014: The turbulence boundary of a temporal jet. *J. Fluid Mech.*, **739**, 254–275, https://doi.org/10.1017/jfm.2013.613.

——, D. Krug, and M. Holzner, 2018: Small-scale entrainment in inclined gravity currents. *Environ. Fluid Mech.*, **18**, 225–239, https://doi.org/10.1007/s10652-017-9514-3.

Watanabe, T., J. Riley, S. de Bruyn Kops, P. Diamessis, and Q. Zhou, 2016: Turbulent/non-turbulent interfaces in wakes in stably stratified fluids. *J. Fluid Mech.*, **797**, R1, https://doi.org/10.1017/jfm.2016.285.

——, X. Zhang, and K. Nagata, 2018: Turbulent/non-turbulent interfaces detected in DNS of incompressible turbulent boundary layers. *Phys. Fluids*, **30**, 035102, https://doi.org/10.1063/1.5022423.

Wyngaard, J., 2010: *Turbulence in the Atmosphere*. Cambridge University Press, 387 pp.